



Deutsches Zentrum  
für Luft- und Raumfahrt  
German Aerospace Center



Universität  
Augsburg  
University

# MASTER'S THESIS

Data-driven parameter identification for processing of Sheet  
Molding Compounds

Oskay Harun Sözen

for obtaining the academic degree *Master of Science*  
in the course *Materials Science and Engineering*.

University of Augsburg  
Faculty of Mathematics, Natural Sciences, and Materials Engineering  
Data-driven Product Engineering and Design

First examiner: Prof. Dr.-Ing. Nils Meyer

Second examiner: Prof. Dr.-Ing. Michael Kupke

Augsburg, September 2025

# Abstract

The reliable simulation of Sheet Molding Compound (SMC) compression molding requires an accurate description of its rheology. Two aspects are particularly critical: non-Newtonian viscosity and wall-slip behaviour. These factors, combined with anisotropic fiber orientation within the polymer, make a complex flow process. Classical rheological methods, such as plate-plate or capillary rheometry, fail to capture this complexity, while modern in-situ rheometers, though more representative, demand elaborate and costly experimental setups. To identify this complex structure with a simpler approach this thesis presents a data-driven parameter identification framework for SMC rheology. The method uses Bayesian Optimization (BO) with Gaussian Process (GP) surrogate modeling, combined with Autodesk Moldflow through a python script to automate the optimization. Experimental force-time curves serve as the reference data, enabling direct calibration of a modified Cross viscosity model and wall slip model under process conditions. The optimization loop was first validated on a reduced two-parameter slip model before being extended to the complete parameter set, including viscosity and slip. The results demonstrate that the framework converges towards parameter sets that minimize the error between simulations and experiments. Overall, the proposed framework provides a scalable methodology for data-driven rheology identification in composite processing, bridging the gap between industrial experiments and process simulations.

# Acknowledgments

This thesis was written in collaboration with the University of Augsburg and the Deutsches Zentrum für Luft- und Raumfahrt (DLR) – Zentrum für Leichtbauproduktionstechnologie (ZLP). I would like to express my sincere gratitude to Prof. Nils Meyer for giving me the opportunity to work at the group, Data-Driven Product Engineering and Design. His guidance, valuable feedback, and inspiring discussions throughout the project have been extremely helpful.

I would also like to thank the DLR for the opportunity to conduct my research within the ZLP. In particular, I am deeply grateful to Dr. Stefan Jarka for his support, constructive advice, and encouragement. My thanks also go to my colleagues at DLR, whose assistance with experiments and insightful discussions greatly contributed to the progress of this work.

Finally, I would like to thank my family and friends for their constant support, patience, and encouragement throughout the course of my studies and this thesis. Without their understanding and motivation, this work would not have been possible.

# Acronyms

<b>SMC</b>	Sheet Molding Compound
<b>BO</b>	Bayesian Optimization
<b>EI</b>	Expected Improvement
<b>LHS</b>	Latin Hypercube Sampling
<b>MSE</b>	Mean Squared Error
<b>GP</b>	Gaussian Process
<b>EI</b>	Expected Improvement
<b>DLR</b>	Deutsches Zentrum für Luft- und Raumfahrt
<b>ZLP</b>	Zentrum für Leichtbauproduktionstechnologie
<b>CEL</b>	Coupled Eulerian–Lagrangian
<b>DBS</b>	Direct Bundle Simulation
<b>CAD</b>	Computer Aided Design
<b>UP</b>	Unsaturated Polyester
<b>CF-SMC</b>	Carbon Fiber-Sheet Molding Compound
<b>PI</b>	Probability of Improvement
<b>UCB</b>	Upper Confidence Bound
<b>ML</b>	Machine Learning
<b>DFT</b>	Density Functional Theory
<b>RBF</b>	Radial Basis Function

# Contents

<b>Abstract</b>	<b>ii</b>
<b>Acknowledgments</b>	<b>iii</b>
<b>1 Introduction</b>	<b>1</b>
<b>2 State of Research</b>	<b>3</b>
2.1 SMC Production . . . . .	3
2.2 SMC Flow Process . . . . .	4
2.2.1 Flow Mechanics . . . . .	5
2.2.2 Simulation Methods . . . . .	6
2.2.3 Characterization . . . . .	7
2.3 Bayesian Optmization . . . . .	14
<b>3 Methodology</b>	<b>18</b>
3.1 Experimental Data Acquisition . . . . .	18
3.2 Rheological Models . . . . .	20
3.2.1 Viscosity Model . . . . .	20
3.2.2 Slip Velocity Model . . . . .	21
3.3 Simulation Framework . . . . .	21
3.3.1 Parameter space and bounds . . . . .	22
3.3.2 Gaussian Process surrogate and optimization . . . . .	23
3.3.3 Automation Pipeline . . . . .	23
<b>4 Results and Discussion</b>	<b>26</b>

4.1	Experimental Reference Data . . . . .	26
4.2	Verification of Optimization in 2D Case . . . . .	31
4.3	Model Training . . . . .	40
4.4	Optimization . . . . .	44
4.5	Validation . . . . .	50
4.6	Comparison with Literature . . . . .	51
<b>5</b>	<b>Conclusions</b>	<b>53</b>
	<b>Bibliography</b>	<b>55</b>

# 1 Introduction

SMCs offers an attractive combination of high specific stiffness and strength, design flexibility, and suitability for high-volume production, making it a competitive alternative to metals and thermoplastics in semi-structural applications. The demand for lightweight, high-performance components in sectors such as automotive, aerospace, and industrial manufacturing led to interest in these products [1, 2]. On the other hand, flow behaviour of SMC during compression molding is highly complex, governed by non-Newtonian, shear thinning viscosity, wall-slip effects, fibre-matrix interaction, and curing kinetics [3–5]. Accurate prediction of this behaviour in numerical simulations is essential for fiber orientation, defects and achieving the desired part performance.

Simulation tools such as Autodesk Moldflow are widely used to model mold filling processes, but the accuracy is directly dependent on the quality of the input rheological parameters. Conventionally, these parameters are obtained from laboratory-scale tests such as squeeze-flow rheometry or shear-compression rheometry [6, 7]. However, these methods often fail to capture the real in-mold behaviour of SMC since they do not replicate the temperature gradients, surface lubrication effects and large scale fiber structures present in actual manufacturing. This limitation has encouraged the development of in-situ methods, where rheology is directly observed from industrial press trials rather than conventional rheometers [8, 9]. These in-line methods need complex rheology tools and sensors in order to predict the parameters accurately. Identifying these parameters in simpler but likewise accurate way would be a great benefit. The objective of this work is to develop and validate a data-driven parameter identification framework for SMC compression molding. The methodology integrates, Autodesk Moldflow simulations and BO. The framework uses force–time and displacement–time curves from multiple press trial configurations as reference data, automates Moldflow simulations through Python scripting and employs a GP surrogate model to iteratively refine parameter sets. The modified Cross viscosity model and Moldflow’s slip velocity model are calibrated

## 1 Introduction

---

simultaneously to minimize the global deviation between simulations and experiments. This approach is designed to produce parameter sets that are valid across different charge shapes, mold coverages, and press speed profiles.

## 2 State of Research

### 2.1 SMC Production

Manufacturing of SMC sheets is a continuous process that uses fibers of 25–50 mm length and a thermosetting matrix. A polymeric foil coated with a resin mixture is laid on a conveyor belt. Carbon or glass fiber bundles are chopped at a cutting unit and distributed onto the resin-coated foil. Another resin-coated foil is then placed on top of the fibers, forming a sandwich structure. This structure is compressed by a series of rollers, after which the sheets are allowed to mature for a certain period of time (from hours to days). During transportation, the sheets are stored at low temperatures.

At the compounding stage, the viscosity of the sheets is kept low to ensure proper impregnation of the fibers. The resin mixture contains fillers, thickeners, and hardeners that increase viscosity later, making the sheets easier to handle [1, 10]. Classical SMC typically uses Unsaturated Polyester (UP) resin diluted with styrene; fillers (often  $\text{CaCO}_3$ ) improve cost/performance; low-profile additives (e.g., thermoplastics) control shrinkage; zinc stearate provides mold release; peroxides act as initiators; and alkaline earth oxides/hydroxides (e.g.,  $\text{MgO}/\text{Mg}(\text{OH})_2$ ) act as thickeners. Epoxy-based Carbon Fiber-Sheet Molding Compound (CF-SMC) variants replace UP/styrene with epoxy matrices and latent hardeners to achieve higher structural performance and paint-shop compatibility [11]. Modern SMC lines integrate in-line metrology to control paste areal weight, fiber areal weight, fiber distribution, and sheet thickness [12].

CF-SMC extends SMC into structural, crash-relevant applications. Recent studies compare epoxy- vs. vinyl-ester-based CF-SMC, investigate low/zero-flow preforms to better control fiber orientation, and integrate virtual process chains to improve prediction of defects and orientation [13].

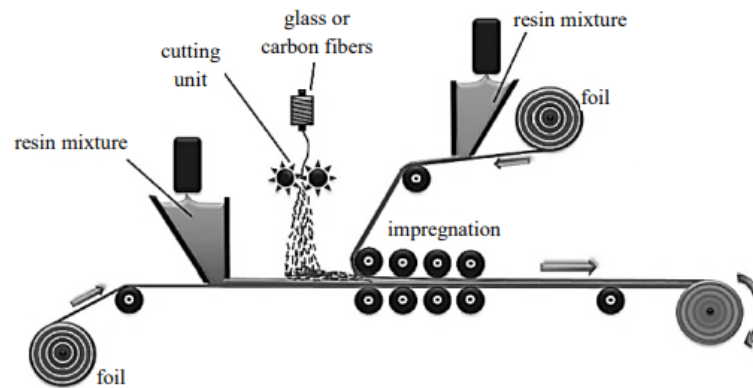


Figure 2.1: Visual representation of sheet production [14].

To manufacture parts from SMC material, compression molding is used. Sheets are cut to the required part shape and placed into a mold, with mold coverage typically ranging from 25% to 100%. The pre-heated mold is closed upon the sheets, allowing them to fill the cavity. The mold closes with a predefined velocity profile, after which the press switches to force control once the target force is reached. The part remains in the mold until it is partially cured and is then released [15].

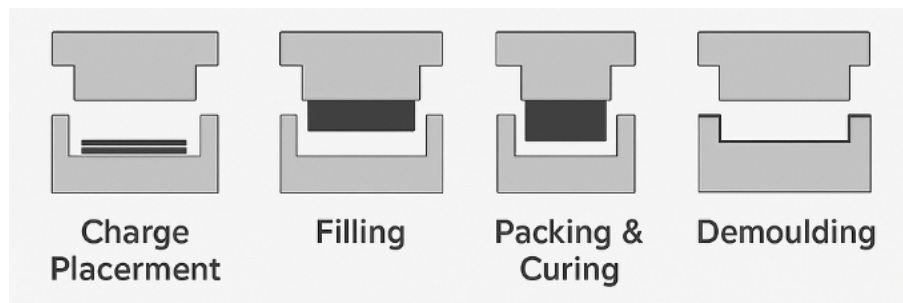


Figure 2.2: Scheme of the SMC molding [16].

## 2.2 SMC Flow Process

The flow behaviour of SMC during compression molding is a complex phenomenon influenced by rheology, microstructure, curing, and interactions between the charge and mold surfaces. Since the flow duration is short (typically 5–15 s), curing is often neglected in flow modeling [5]. The following subsections review the understanding of flow mechanics, the development of simulation methods, and experimental characterization techniques.

### 2.2.1 Flow Mechanics

Barone and Caulk investigated the flow behaviour of thin SMC layers and observed that, although strong resistance to transverse shearing was expected due to fiber interlocking, considerably less resistance to extensional flow occurred because of the short fiber lengths [17]. Silva-Nieto et al. later developed a simplified flow model that assumed Newtonian behaviour, negligible fiber reorientation, no wall slip, and a thin stagnant layer at the mold surface, with the material flowing in layers [18].

In contrast, Lee et al. emphasized the non-Newtonian, shear-thinning, and viscoelastic nature of SMC. They described the shear viscosity using the Carreau model (Eq. 2.1):

$$\frac{\eta - \eta_{\infty}}{\eta_0 - \eta_{\infty}} = [1 + (\lambda\dot{\gamma})^2]^{(n-1)/2} \quad (2.1)$$

where  $\eta_0$  is the zero-shear viscosity,  $\eta_{\infty}$  the viscosity at infinite shear rate,  $\lambda$  a time constant, and  $n$  the power-law index. This formulation allowed experimental data to be reduced to a single master curve. Their work also revealed the phenomenon of *thermal lubrication* (Fig. 2.3), in which the hot mold surface induces a low-viscosity layer that lubricates the bulk, enabling easier flow of the surface layers [3].

Building on this, Barone and Caulk performed experiments with black-and-white charge layers to directly visualize flow kinematics 2.4. They showed that SMC charges deform primarily by uniform extension within layers, with slip occurring at the mold surface (Fig. 2.4) [4]. Lee and Tucker confirmed the existence of the thin, lubricating surface layer, which facilitated planar elongational deformation of the bulk charge [19].

Later, Odenberger et al. visualized flow fronts during compression molding with high-resolution monitoring and identified three distinct phases:

- *Squish*: complex flow where air can be entrapped and SMC near mold surfaces moves faster than the bulk.
- *Flow*: a stable plug-flow regime.
- *Boiling*: bubble formation in low-pressure zones, likely due to styrene evaporation.

Their work (Fig. 2.5) supported earlier observations by Barone and Caulk and highlighted that plug flow provides a better description of SMC behavior than generalized Hele-Shaw models that exclude slip at mold surfaces [4, 20–22].

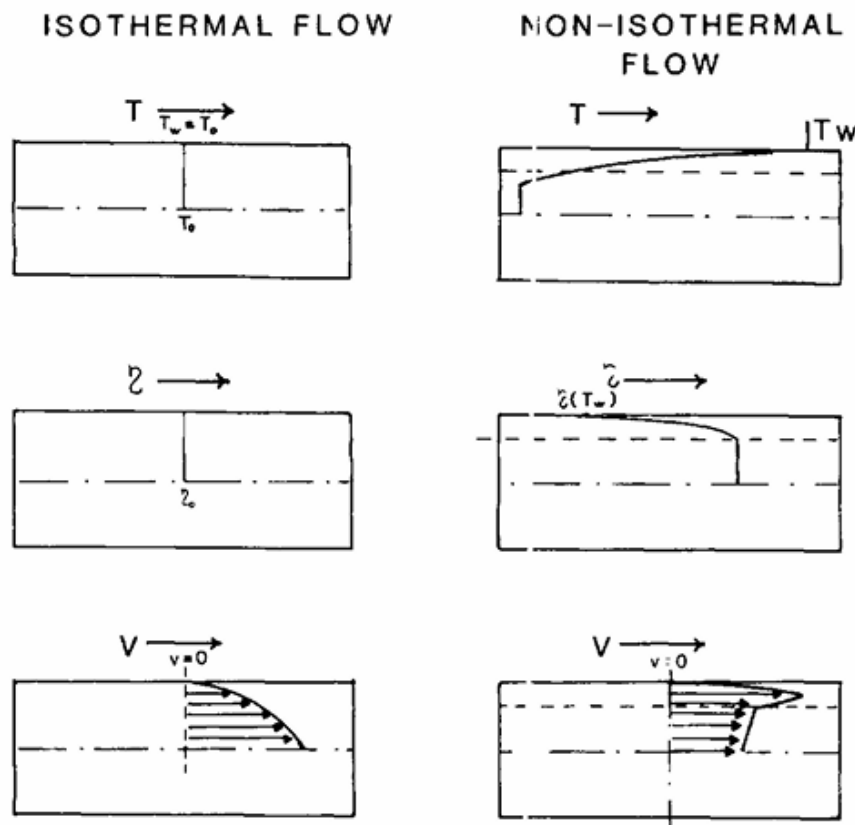
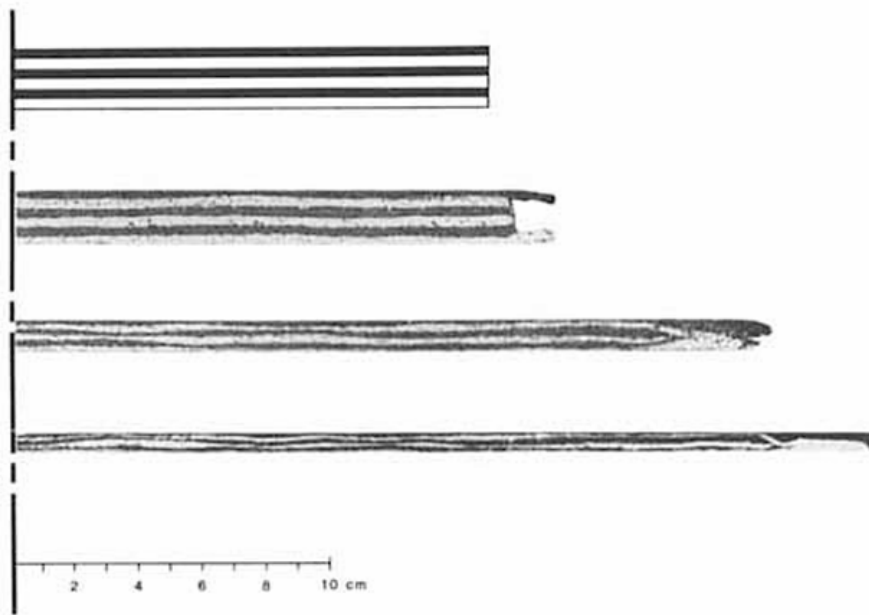


Figure 2.3: Effect of heat transfer on flow pattern [3].

### 2.2.2 Simulation Methods

The development of flow simulation models began with Tucker and Folgar, who applied the Hele-Shaw model to compression mold filling of thin parts [21, 23]. Their approach assumed isothermal Newtonian flow and no slip at mold walls, providing a simplified framework solved using the finite element method. Although limited, this work laid the foundation for more advanced approaches.

Barone and Osswald later proposed a boundary element method to address anisotropy and observed kinematics [24]. By treating SMC as a membrane-like sheet undergoing uniform extension with slip at the mold surface, their method represented a significant departure from lubrication-based theories. Around the same time, Osswald and Tucker developed a finite element–control volume hybrid scheme to simulate mold filling. This method divided the domain into control volumes, enabling the handling of complex geometries while maintaining global mass balance. Flow fronts were approximated but could be refined through post-processing (Fig. 2.6) [25].



**Figure 2.4:** Investigation of flow mechanism with contrast-colored charge layers [4].

With increasing computational power, more advanced techniques emerged. In the late 2010s, Görthofer et al. implemented Coupled Eulerian–Lagrangian (CEL) simulations in Abaqus to capture 3D mold filling, pressure build-up, and fiber orientation evolution. These simulations provided input for structural analyses as part of a Virtual Process Chain [26]. Alnersson et al. reviewed the state of numerical methods, highlighting difficulties in predicting flow and pressure evolution in high-fiber-content SMC, and emphasizing the role of anisotropic viscosity [27].

Commercial tools such as Autodesk Moldflow and Moldex3D, while widely applied, were originally developed for injection molding and had limited validation for reactive compression molding at the time of publication [28]. To overcome limitations of continuum-based models, Meyer et al. introduced the Direct Bundle Simulation (DBS) approach, which explicitly represents fiber bundles as truss-like segments coupled with the fluid. This two-way coupling allows flow, fiber motion, and orientation to emerge naturally from the simulation physics (Fig. 2.7) [29, 30].

### 2.2.3 Characterization

Accurate modeling of SMC flow requires reliable material parameters. Kostikos et al. investigated the flow behaviour of the SMCs using parallel circular plates at various temperatures (Fig. ?? [31]).



**Figure 2.5:** Flow front progression during compression molding [20].

Early investigations therefore relied on squeeze flow rheometers, in which parallel circular plates compress the sample (Fig. 2.9). Material parameters can be derived from press force and displacement measurements using generalized Hele-Shaw models [22]. However, since these models neglect wall slip, errors in the determined material properties may result [3].

Subsequent studies showed that representative rheological data can only be obtained when the sample dimensions are large compared to fiber length. In particular, homogeneous strain fields within SMC are achieved only for specimens exceeding 100 mm in size; smaller samples yield inaccurate results [6, 7]. This motivated the development of custom press rheometers.

Le Corre et al. introduced a shear-compression rheometer (Fig. 2.10), which allowed characterization of samples with varying fiber fractions, temperatures, and strain rates [6]. Lubricated mold surfaces were used to simulate slip conditions. The results indicated that SMC paste behaves as a power-law fluid, but with pronounced anisotropy: shear viscosity was less sensitive to fiber fraction than compressive viscosity.

Another approach is the plain strain rheometer (Fig. 2.11), which reduces flow to a quasi-one-dimensional condition. Dumont et al. used this method to compare mechanical loadings and concluded that the power-law exponent of the material remained consistent across compression and plain-strain modes [7]. However, these tools are

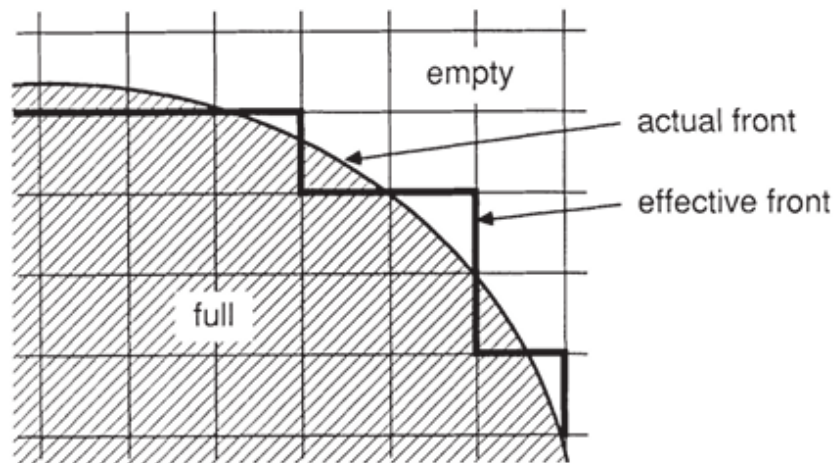


**Figure 2.6:** Actual and effective flow front during compression molding [25].

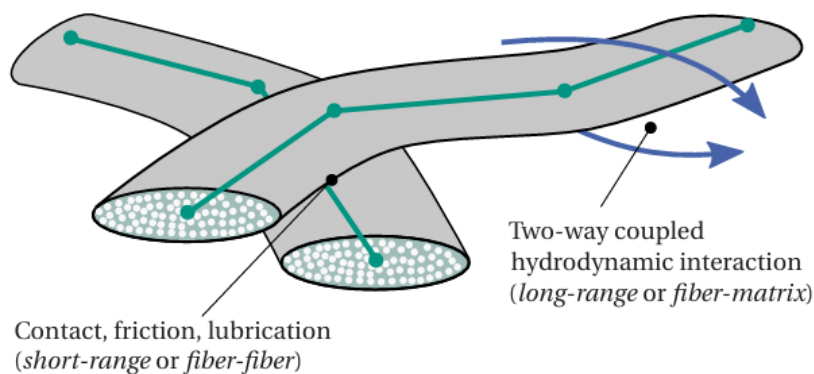


**Figure 2.7:** Visual representation of bundle–bundle and bundle–matrix interactions in the DBS approach [30].

not sufficient for SMC, since their flow conditions differ significantly from in-mold compression flow.

Guiraud et al. later developed an instrumented compression rheometer with advanced capabilities [8]. The device, mounted on a 20 kN press, used two polished plates (200 mm radius) to form a 10 mm cavity. It incorporated heating and cooling systems for precise thermal control, as well as five piezoelectric stress sensors distributed radially across the lower plate. This setup enabled simultaneous measurement of intrinsic rheology, compressibility, and friction forces at the mold–composite interface.

More recently, Hohberg addressed limitations of plain-strain devices, which typically require multiple tests with different charge positions (Fig. 2.12). By embedding pressure

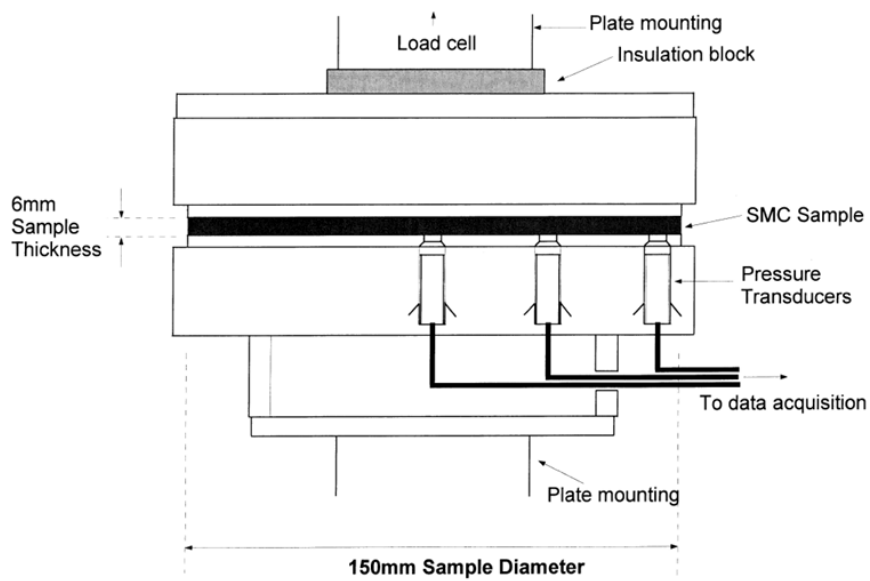


Figure 2.8: Squeeze flow die [31].

sensors directly into the lower mold half, his system continuously measured local pressures during molding. Combined with internal press data (force and displacement), this allowed more robust rheological characterization from a single experiment [32]. Together with visualization techniques, such as high-resolution flow-front monitoring (Fig. 2.13) [27], these rheological tools have established that SMC exhibits non-Newtonian, anisotropic, and slip-dependent behaviour. They provide essential input for validating and refining flow models.

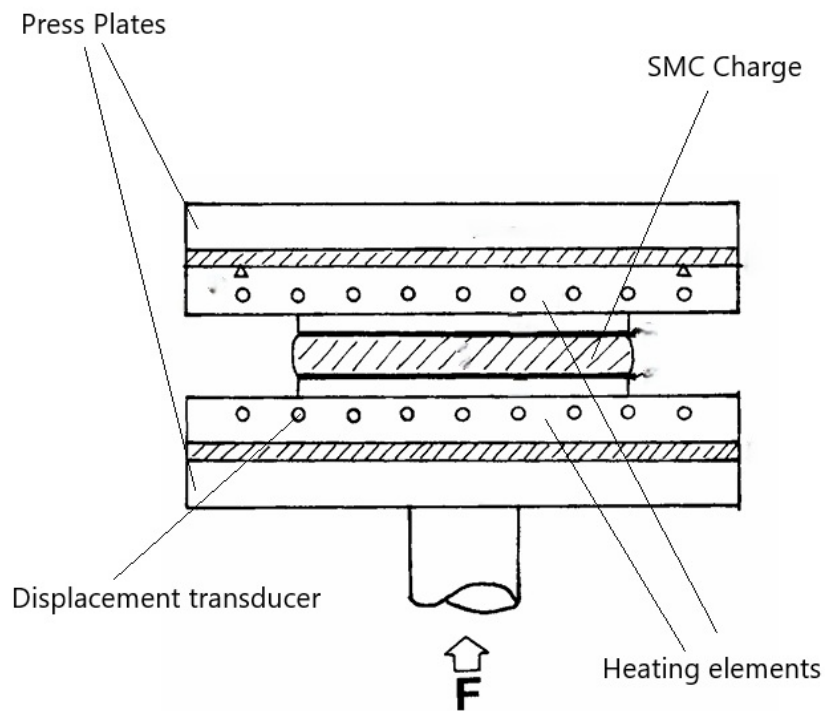


Figure 2.9: Squeeze flow rheometer [3].

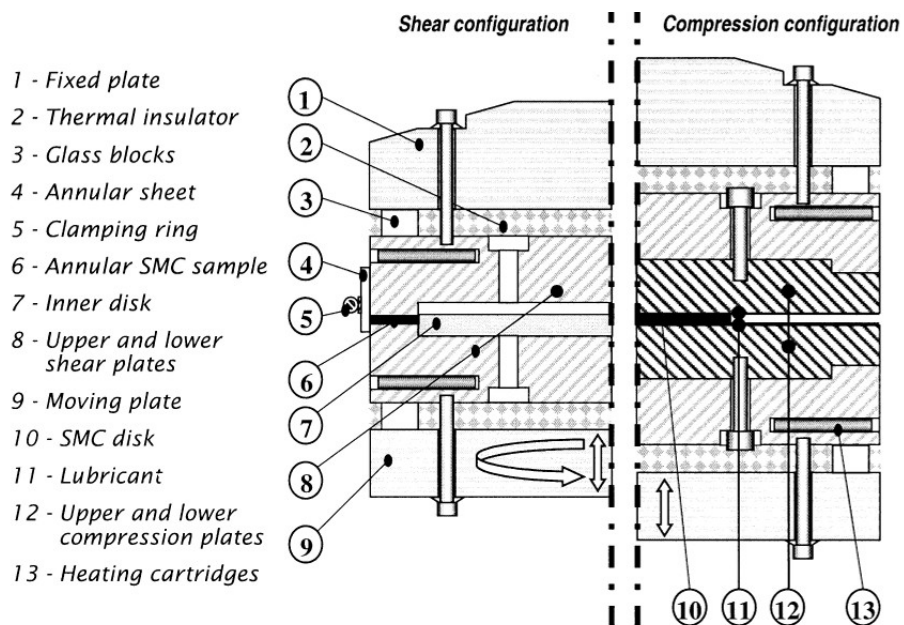


Figure 2.10: Shear-compression rheometer [6].

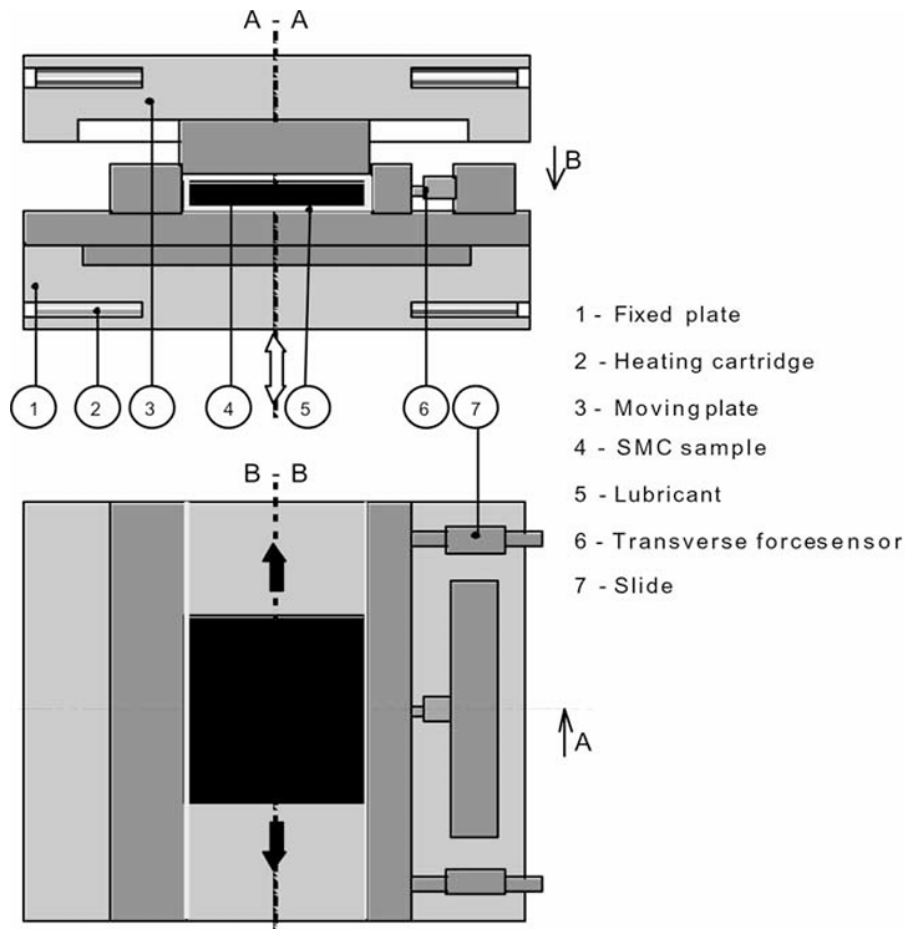


Figure 2.11: Plain strain rheometer [7].

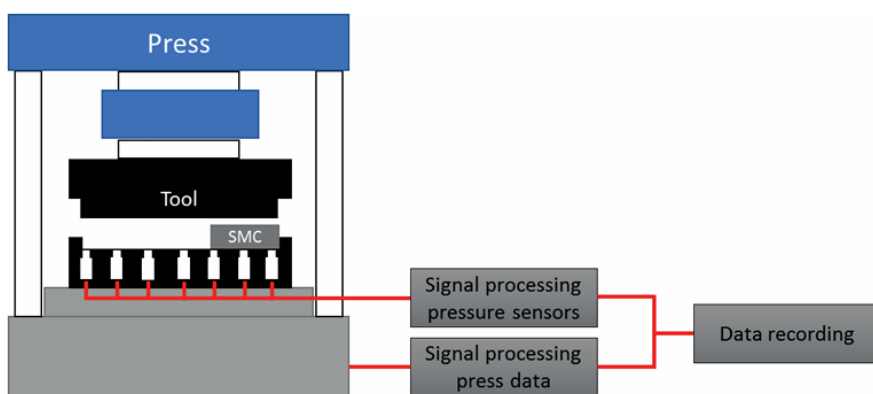


Figure 2.12: Plain strain rheometer with embedded pressure sensors [32].



**Figure 2.13:** Flow front captured by high-resolution cameras [27].

## 2.3 Bayesian Optimization

The increasing availability of computational power and data-driven approaches has also had an impact on natural sciences. Machine Learning (ML) methods in particular are becoming feasible for linking processing conditions, structure, and properties of materials. Instead of relying solely on experimentation or high-fidelity simulations, ML provides surrogate models that can interpolate across large parameter spaces, thereby accelerating characterization. Recent studies have emphasized how ML enables design, synthesis, and prediction of material properties in domains ranging from energy storage to structural alloys [33]. One of the main challenges in applying ML to materials problems is the scarcity of experimental data, since laboratory measurements and simulations are often expensive and time-consuming. While deep learning methods usually require large datasets, probabilistic approaches such as GP are particularly well suited for small-data regimes. GP not only provides predictions but also quantifies the uncertainty of those predictions, which can then be exploited in active learning. Sourroubille et al. demonstrated this by combining GP with rheological experiments to characterize the thermogelation of methylcellulose, showing that the number of experimental runs required could be significantly reduced [34].

BO builds directly on this principle. By combining a surrogate model such as a GP with an acquisition function, BO systematically proposes new experiments or simulations that balance exploration of unknown parameter regions with exploitation of promising candidates. Ziatdinov et al. utilized BO to accelerate scanning probe microscopy, where the algorithm adaptively guided the measurement process in real-time, significantly reducing the data acquisition burden [35]. In another study, BO was employed to optimize material compositions for high-entropy alloys [36]. Moosavi et al. used GP to predict the heat capacity of nanoporous materials such as zeolites and metal-organic frameworks, achieving high accuracy with Density Functional Theory (DFT) training data and revealing local atomic contributions to thermal properties [37].

BO is a method based on Bayes' Theorem, first published in 1763 by Thomas Bayes, which allows one to update beliefs about the objective function based on prior knowledge and new observations [38]. Bayes' Theorem is expressed as

$$p(f | \mathcal{D}) = \frac{p(\mathcal{D} | f) \cdot p(f)}{p(\mathcal{D})}, \quad (2.2)$$

where:

- $p(f | \mathcal{D})$  is the posterior distribution of the function given the observed data  $\mathcal{D}$ ,
- $p(\mathcal{D} | f)$  is the likelihood, representing the probability of observing the data given the function  $f$ ,
- $p(f)$  is the prior belief about the function  $f$  before observing any data,
- $p(\mathcal{D})$  is the marginal likelihood or evidence.

BO is an efficient method for finding the global optimum for black-box functions, especially suitable when evaluations are costly and noisy [39]. BO uses probabilistic modeling with a decision theory, making informed choices on where to sample next. Thus, optimizing performance with fewer evaluations [40]. It is a probabilistic approach to optimize objective functions that are longer (expensive) to evaluate. Typically, it works best for problems with dimensions lower than 20 [41]. This method focuses on solving the problem

$$\max y(x)$$

where  $y$  is the expensive objective function to evaluate.

BO revolves around two primary components:

- **Surrogate Model:** A GP model is used to approximate the objective function. A GP provides a probabilistic framework that offers both a prediction and an uncertainty estimate for any input point. The model outputs a predictive distribution for new points, offering an expected value and a quantifiable measure of uncertainty, guiding the optimization process effectively [42].
- **Acquisition Function:** Determines the next sampling point by balancing exploration of uncertain areas and exploitation of known promising regions. Common acquisition functions include Expected Improvement (EI), Probability of Improvement (PI), and Upper Confidence Bound (UCB) [39].

EI is one of the most used acquisition functions in BO. It measures the expected increase in the objective function value compared to the current best observation. Mathematically, for a fully sequential (evaluating one point at a time,  $q=1$ ) and single outcome (optimizing a single objective,  $M=1$ ) setting, EI is described as:

$$\text{EI}_{y^*}(x) = \mathbb{E}_{f(x)} [[f(x) - y^*]_+] = \sigma(x)h\left(\frac{\mu(x) - y^*}{\sigma(x)}\right) \quad (2.3)$$

where  $y^*$  is the best function value observed so far,  $\mu(x)$  and  $\sigma(x)$  are the mean and standard deviation of the GP posterior prediction at point  $x$ , respectively. Figure 2.14 shows the first step of a Bayesian Optimization process. The unknown objective function

(orange) evaluated at points (black) and confidence interval (light blue) computed. Here, a probabilistic model of our objective function has been built and with the acquisition function, it has been decided where to sample next. Figure 2.14 shows the acquisition function evaluation for the GP model. Points where previous observations were located valued lowest and with balancing exploration and exploitation it chooses where to sample next, which has the highest value [43]. In Figure 2.16, one can see the updated GP model and the best observed value so far.

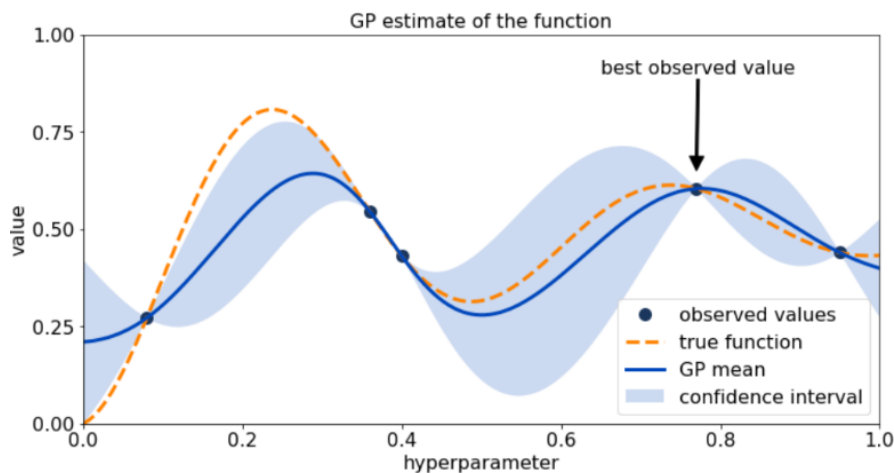


**Figure 2.14:** Plot of the GP model with ground truth and confidence interval [43].

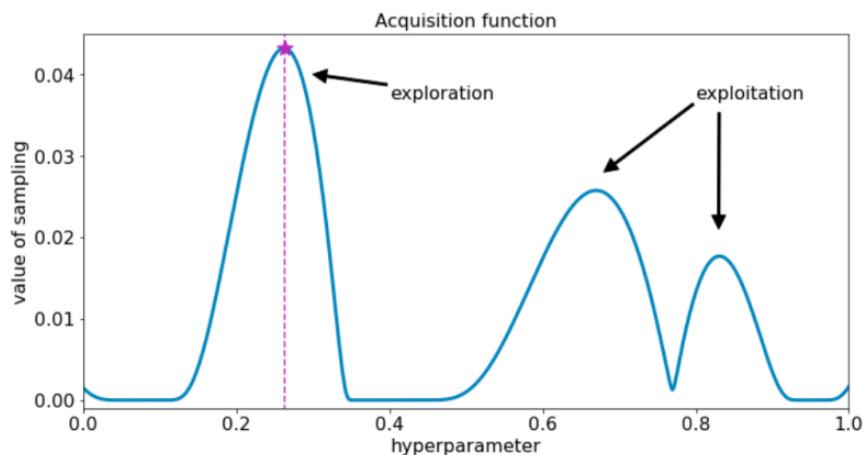


**Figure 2.15:** Plot of the acquisition function with exploration and exploiting areas [43].

A recent study from Ament et al. highlighted issues in numerically optimizing EI, notably due to vanishing gradients [44]. The LogEI family of acquisition functions rep-

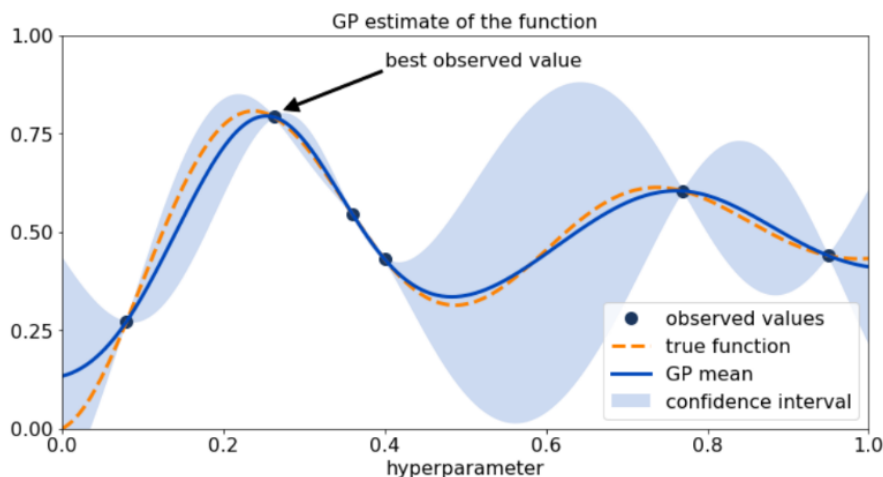


Figure 2.16: GP Model with updated information [43].

resents an advancement in addressing the numerical instabilities inherent in traditional EI. Its design principles, centered on log-transformation (numerically stable implementation of  $\log(h(z))$ ) and approximations, effectively overcome the vanishing gradient problems. The logarithmic transformation ensures that the values and gradients do not vanish numerically, facilitating a more effective gradient-based optimization. This development is especially useful in high-dimensional spaces, constrained optimization problems, and problems with a large number of evaluations, where traditional EI can struggle [44]. The LogEI acquisition function is defined as:

$$\text{LogEI}_y(x) = \log h \left( \frac{\mu(x) - y}{\sigma(x)} \right) + \log(\sigma(x)) \quad (2.4)$$

The rheological characterization of SMCs is essential for the flow prediction and process parameters of parts. As stated in the literature, although there is a small amount of flow time, there is a complex flow process, which is paramount for the quality of the end product. Simulation of the mold filling process requires calibration of these parameters, which dictates the mechanisms at work. Existing experimental techniques such as in-situ rheometers include complex setups and qualified personnel to predict those parameters. This work aims to introduce a data-driven method that utilizes a machine learning algorithm to inversely characterize the rheological parameters. Compared to predecessors, this method requires simple test rigs but also an intricate data treatment and simulation process. This trade-off is encouraging in the ever-improving digital world with more powerful and efficient computing resources becoming available.

## 3 Methodology

In this chapter, the methodological framework employed for the data-driven parameter identification of SMC compression molding is outlined. The method combines software simulations with Bayesian optimization to identify viscosity and wall slip parameters that minimize the error between simulated and experimental press force and press displacement against time curves. The method employs a closed-loop framework, in which a Bayesian optimization algorithm proposes candidate parameters, which are evaluated via simulations in Autodesk Moldflow and compared to reference press data obtained at DLR-ZLP. The optimization objective is defined as Mean Squared Error (MSE) between the experimental and simulated curves. The process consists of the following stages:

- Experimental press trials to obtain reference force, displacement–time data.
- Definition of rheological models and parameter bounds for viscosity and wall slip.
- Setup and execution of Moldflow compression molding simulations.
- Post-processing of simulation outputs to extract press force–time curves.
- Computation of the objective function (MSE).
- Bayesian optimization loop to iteratively propose improved parameter sets.

### 3.1 Experimental Data Acquisition

The reference data were obtained from compression molding trials conducted on a Wickert WKP 4400S hydraulic press (Figure 3.1). A 305×305 mm mold was used for all press trials. Trials were performed under four different charge configurations and three different closing speeds, as shown in Figure 3.2.



**Figure 3.1:** Wickert WKP 4400S industrial hydraulic press.

The mold was lubricated with Loctite 700-NC release agent before each press process. The mold temperature was kept at 135°C for all samples. The press was operated in speed control mode until the target force limit of 1400 kN was reached. Upon reaching this limit, the press automatically switched to force control mode, maintaining the target force until the end of the process. All trials were performed using Polynt-SMCarbon® 90 CF60-3K, a sheet molding compound based on epoxy resin and reinforced with 60% wt. carbon fiber content (3K fiber tow, 25 mm length). The charges consisted of four layers, all cut by hand from the material roll. These initial charges were weighed on a scale for thickness and spillage calculations. For each configuration  $k$ , an experimental master curve  $F_k^{\text{exp}}(t)$  was obtained from press sensor data, post-processed, and stored as CSV file.

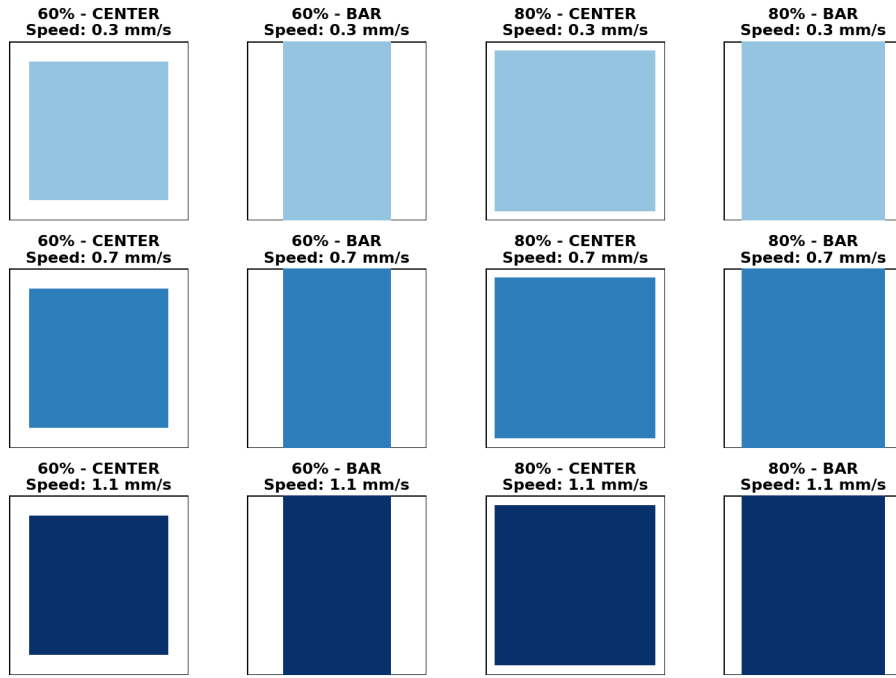


Figure 3.2: Press configurations with varying speeds and mold coverages.

## 3.2 Rheological Models

As mentioned in the second chapter, in order to understand the rheology of the SMCs, the flow process must be analyzed. This flow process is influenced both by the viscosity of the material and the wall-slip parameters, since slip conditions are present. Autodesk Moldflow allows both parameters to be simulated with its built-in and user-defined functions.

### 3.2.1 Viscosity Model

In this work, the viscosity of the SMC material is defined using a modified Cross model that accounts for curing degree, temperature, and shear rate. The viscosity is given by

$$\eta(\alpha, T, \dot{\gamma}) = \frac{\eta_0(T)}{1 + \left(\frac{\eta_0(T)\dot{\gamma}}{\tau^*}\right)^{1-n}} \left(\frac{\alpha_g}{\alpha_g - \alpha}\right)^{c_1+c_2\alpha}. \quad (3.1)$$

In this model, the viscosity depends on the curing degree  $\alpha$ , the processing temperature  $T$ , and the applied shear rate  $\dot{\gamma}$ . The critical stress level at the transition to shear thinning is represented by  $\tau^*$ , while  $n$  is the power-law index controlling the rate of viscosity decrease with increasing shear rate. The effect of curing is governed by the constants  $c_1$  and  $c_2$ , which describe the rate of viscosity increase as curing progresses. Since no

significant curing was assumed during the flow process, these two constants were set to zero in order to exclude the effect of curing from the calculations.

The zero-shear viscosity  $\eta_0(T)$  represents the viscosity at very low shear rate and is temperature dependent. This expression establishes the baseline viscosity from which shear thinning begins. It follows an Arrhenius-type relationship:

$$\eta_0(T) = B \exp\left(\frac{T_b}{T}\right) \quad (3.2)$$

Here,  $B$  is a pre-exponential factor and  $T_b$  is an activation temperature constant. This relation captures the strong viscosity decrease with increasing temperature, which is typical for thermosetting resins [45, 46]. To avoid non-unique solutions in the optimization process,  $T_b$  was kept fixed and only the pre-exponential factor  $B$  was calibrated.

#### 3.2.2 Slip Velocity Model

The slip velocity at the mold–material interface in SMC compression molding is modeled using a modified power-law relationship with a threshold at a critical wall shear stress. This formulation, implemented in Autodesk Moldflow, is given by

$$v_s = \frac{\alpha}{1 + \left(\frac{\tau_c}{\tau_w}\right)^{10}} \tau_w^m, \quad (3.3)$$

where  $v_s$  is the slip velocity,  $\tau_w$  is the wall shear stress, and  $\tau_c$  is the critical shear stress above which slip occurs. For  $\tau_w < \tau_c$ , the denominator suppresses slip, reflecting observations where material adheres to the mold surface until a threshold is reached. The slip exponent  $m$  governs how sensitively the slip velocity increases with  $\tau_w$  in the power-law regime. The slip coefficient  $\alpha$  is a scaling parameter that sets the overall magnitude of the slip velocity once  $\tau_c$  is reached [47].

### 3.3 Simulation Framework

Compression molding simulations were performed in Autodesk Moldflow, which models the mold geometry, charge placement, mold temperature, velocity profiles, force limit, and press control strategy from the experimental trials. Computer Aided Designs (CADs) of the mold and the initial charges were created with Autodesk Inventor and imported into Moldflow (Fig. 3.3). The simulation model was configured to allow wall-slip calculations and user-defined viscosity calculations, which enable modification

of the material's viscosity parameters via scripting. The latter feature is only available in the 2026 version of Moldflow for the Reactive Compression Molding process type.

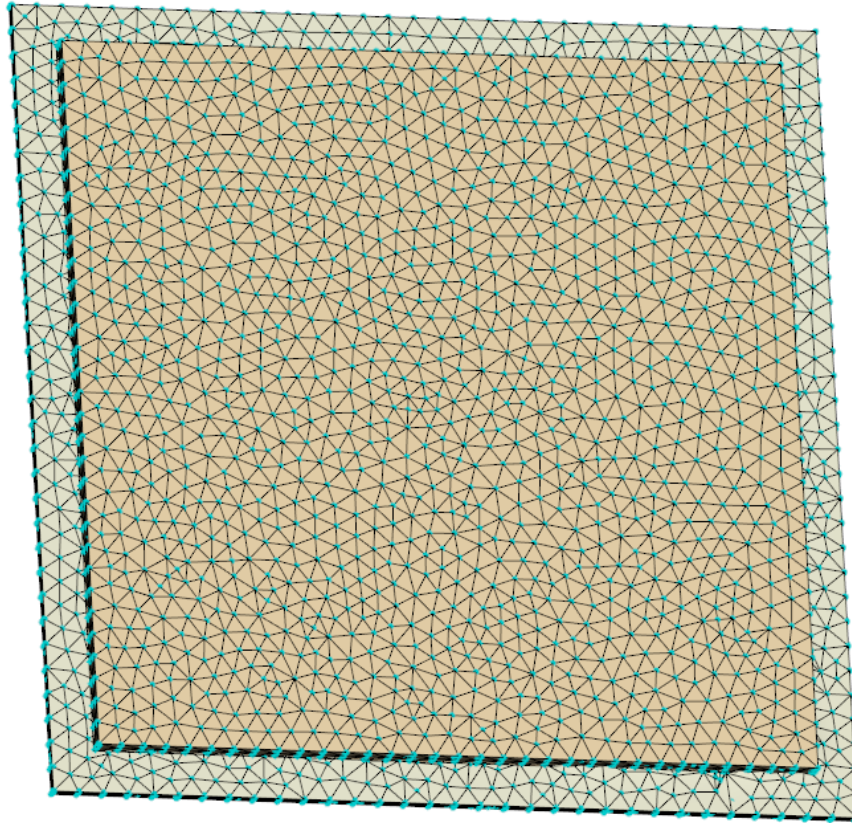


**Figure 3.3:** Compression molding CAD model. The part below represents the final part, and the part above it is the initial charge.

#### 3.3.1 Parameter space and bounds

The optimization vector includes the viscosity and wall-slip parameters used in this work

$$\psi = \{n, B, \tau_w, \tau^*, m\}. \quad (3.4)$$

Practical lower and upper bounds were set from literature and pilot runs to keep the viscosity range typical for SMCs. To avoid surrogate bias from the initial settings, an Latin Hypercube Sampling (LHS) was used to sample the initial parameter space for the GP model. The optimization begins with ten generated parameter sets within the specified bounds. For each parameter set  $\psi$ , the material data are updated and simulations are

executed for each training configuration. Force–time and displacement–time curves,  $F_k^{\text{sim}}(t; \psi)$  and  $D_k^{\text{sim}}(t; \psi)$ , are aligned in time with their experimental counterparts and interpolated to a common grid. The per-configuration mean squared error (MSE) is calculated as:

$$e_k^{\text{F}}(\psi) = \frac{1}{N} \sum_{i=1}^N [F_k^{\text{sim}}(t_i; \psi) - F_k^{\text{exp}}(t_i)]^2 \quad (3.5)$$

$$e_k^{\text{D}}(\psi) = \frac{1}{N} \sum_{i=1}^N [D_k^{\text{sim}}(t_i; \psi) - D_k^{\text{exp}}(t_i)]^2 \quad (3.6)$$

The global loss is then computed by averaging the MSE across training configurations  $p$ :

$$\mathcal{L}(\psi) = \frac{1}{p} \sum_{k=1}^p [w_{\text{F}}, e_k^{\text{F}}(\psi) + w_{\text{D}}, e_k^{\text{D}}(\psi)] \quad (3.7)$$

where  $w_{\text{F}}$  and  $w_{\text{D}}$  are weighting coefficients that control the relative importance of the force–time and displacement–time curves. This single scalar  $\mathcal{L}(\psi)$  is what the optimizer uses to compare candidates.

#### 3.3.2 Gaussian Process surrogate and optimization

GP surrogate model is trained on the initial  $(\psi, \mathcal{L}(\psi))$  pairs. The GP outputs both the predicted mean loss and the associated uncertainty for unexplored areas. The LogEI acquisition function selects the next candidate  $\psi'$  by maximizing the potential improvement over the current best loss. For each new candidate  $\psi'$ , training configurations are simulated and the dataset  $(\psi, \mathcal{L}(\psi'))$  is updated, thus the GP model is retrained. This process repeats until the iteration budget is reached or the improvement in  $\mathcal{L}(\psi)$  falls below a predefined value.

#### 3.3.3 Automation Pipeline

A side contribution of this thesis is the development of an automation pipeline that enables the integration of process simulations with Bayesian optimization. This pipeline links Moldflow to a Python-based optimization framework, allowing for iterative parameter identification without manual intervention. The overall workflow can be summarized with the following diagram.

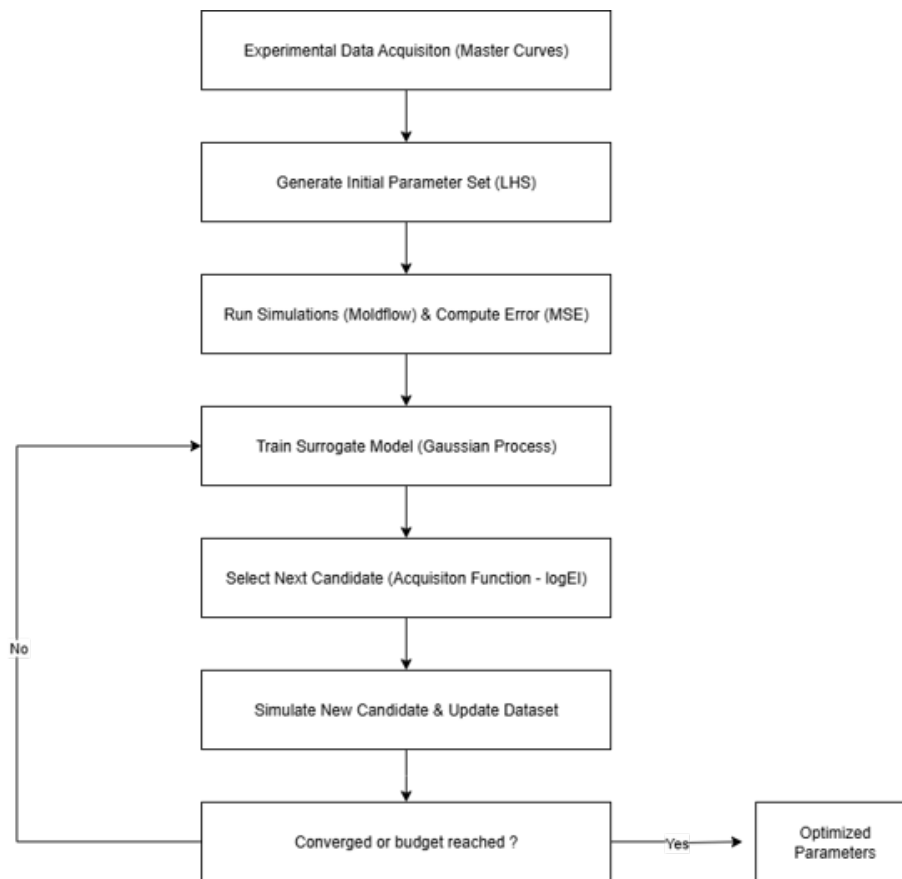


**Figure 3.4:** Diagram of the complete optimization workflow.

The optimization loop itself is implemented in Python, using the `BOTORCH` package for surrogate modeling and acquisition functions, and the `NUMPY` library for numerical operations [48, 49]. `BOTORCH` provides the GP regression framework and acquisition strategies such as `LogExpectedImprovement`, while `NUMPY` is used for efficient vectorized calculations and data preprocessing. The design makes the pipeline both modular and scalable. Each iteration is fully automated: parameter selection, Moldflow execution, data extraction, and optimization update are handled without user input. In this way, a large number of simulations can be executed in sequence, enabling the BO process to efficiently converge toward parameter values that best reproduce experimental press force–time curves. By establishing this automation pipeline, the thesis demonstrates how data-driven optimization can be embedded directly into simulation software. The pseudocode for the complete pipeline is provided in Algorithm 1, and the implementation is available on the project’s GitHub repository<sup>1</sup>.

<sup>1</sup>[https://github.com/oskay-sozen/moldflow\\_automation](https://github.com/oskay-sozen/moldflow_automation)

---

**Algorithm 1** Pseudocode for the Bayesian Optimization Pipeline

---

- 1: **Input:** Parameter bounds, experimental force–time curves  $F_k^{\text{exp}}(t)$ , experimental displacement–time curves  $D_k^{\text{exp}}(t)$  for  $k = 1, \dots, p$
- 2: **Hyperparameters:** Weights  $w_F, w_D$ , number of initial samples  $N_{\text{init}}$
- 3: Generate  $N_{\text{init}}$  initial parameter sets  $\{\psi_i\}_{i=1}^{N_{\text{init}}}$  using LHS
- 4: **for each**  $\psi_i$  in initial set **do**
- 5:     Update Moldflow material parameters  $\psi_i$
- 6:     **for each configuration**  $k = 1, \dots, p$  **do**
- 7:         Run Moldflow simulation for configuration  $k$
- 8:         Extract simulated curves  $F_k^{\text{sim}}(t)$  and  $D_k^{\text{sim}}(t)$
- 9:         Align and interpolate simulated and experimental curves to a common time grid
- 10:         Compute force MSE:

$$e_k^F(\psi_i) = \frac{1}{N} \sum_{j=1}^N [F_k^{\text{sim}}(t_j) - F_k^{\text{exp}}(t_j)]^2$$

- 11:         Compute displacement MSE:

$$e_k^D(\psi_i) = \frac{1}{N} \sum_{j=1}^N [D_k^{\text{sim}}(t_j) - D_k^{\text{exp}}(t_j)]^2$$

- 12:         Compute global loss:

$$\mathcal{L}(\psi_i) = \frac{1}{p} \sum_{k=1}^p [w_F e_k^F(\psi_i) + w_D e_k^D(\psi_i)]$$

- 13:         Store  $(\psi_i, \mathcal{L}(\psi_i))$
  - 14: Fit GP surrogate model to collected data
  - 15: **while** stopping criteria not met **do**
  - 16:     Select next candidate  $\psi'$  by maximizing LogEI
  - 17:     Update Moldflow material parameters with  $\psi'$
  - 18:     **for each configuration**  $k = 1, \dots, p$  **do**
  - 19:         Run Moldflow simulation for configuration  $k$
  - 20:         Compute  $e_k^F(\psi')$  and  $e_k^D(\psi')$  as above
  - 21:         Compute  $\mathcal{L}(\psi')$  as above
  - 22:         Append  $(\psi', \mathcal{L}(\psi'))$  to dataset
  - 23:         Retrain GP model
  - 24: **Output:** Optimal parameters  $\psi^*$  with minimal global loss
-

## 4 Results and Discussion

The trials were performed under twelve distinct process configurations, combining three mold closing speeds, two initial surface coverages, and two charge shapes (see Figure 3.2). For all trials, the force limit was set to 1400 kN; upon reaching this threshold, the press automatically switched from speed control to force control and maintained the target force until the end of the cycle. During each trial, the press was instrumented to record force and displacement signals over time. The data were collected at high frequency through the integrated sensor system and exported as CSV files for further processing. These curves served as master data in the automated optimization loop implemented in Python.

### 4.1 Experimental Reference Data

Raw signals underwent post-processing steps including trimming of idle press states, alignment of time zero with mold closure initiation, and filtering to remove high-frequency noise. The resulting force–time and displacement–time curves represent the reference master curves for the simulation–experiment comparison. Results for the twelve configurations are shown in Figures 4.1–4.4, where both force–time and displacement–time curves are plotted. The displacement curves begin at the point where the press reached the maximum force limit of 1400 kN and switched from speed control to force control. It can be seen that the flow process was dominated by force-controlled conditions, and displacement exhibited only marginal changes over a long period of time compared to the force-controlled section of the process. Because the displacement response does not provide significant additional information for distinguishing parameters, its contribution to the objective was intentionally suppressed. To do so in (3.7),  $w_F = 1$  and  $w_D = 0$  were set. This ensures that the optimization focuses solely on experimentally measured force evolution, which is sensitive to changes in the viscosity and slip parameters.

## 4 Results and Discussion

Figures 4.1–4.4 illustrate typical trends across the tested conditions. Higher closing speeds (0.7 and 1.1 mm/s) led to a much steeper force build-up, whereas lower speeds (0.3 mm/s) produced smoother force curves with delayed peaks. Differences between initial surface coverages (60% versus 80%) and charge placements (CENTER versus BAR) are also reflected in the slope and curvature of the force response. These variations across configurations help the optimization process balance the discrepancies under diverse molding conditions.

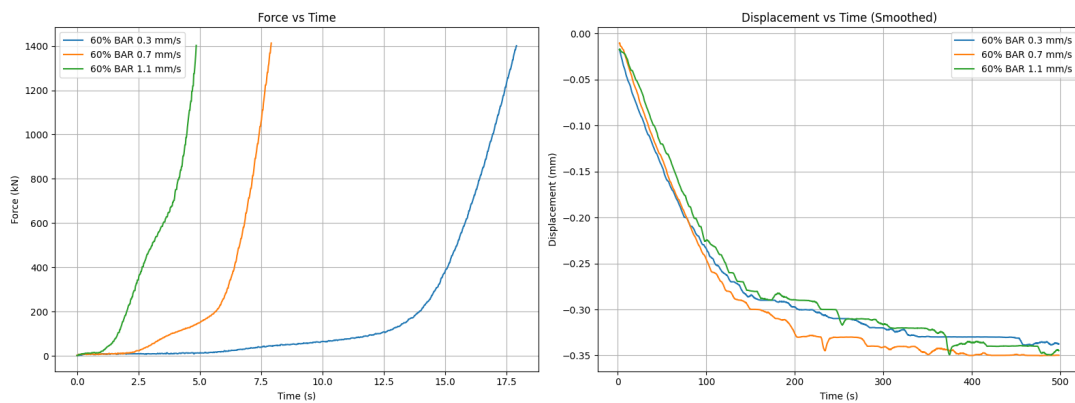


**Figure 4.1:** Force–time (left) and displacement–time (right) for 60% CENTER charge at three closing speeds (0.3, 0.7, 1.1 mm/s).

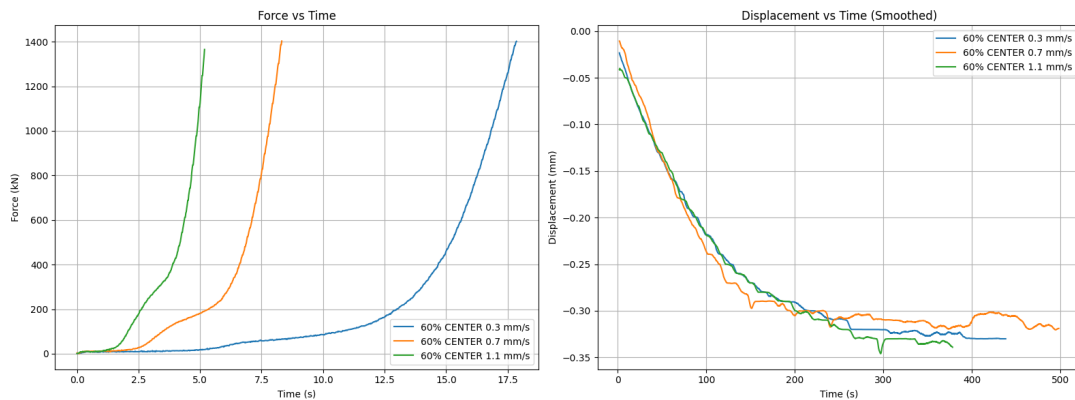


**Figure 4.2:** Force–time (left) and displacement–time (right) for 80% BAR charge at three closing speeds (0.3, 0.7, 1.1 mm/s).

## 4 Results and Discussion

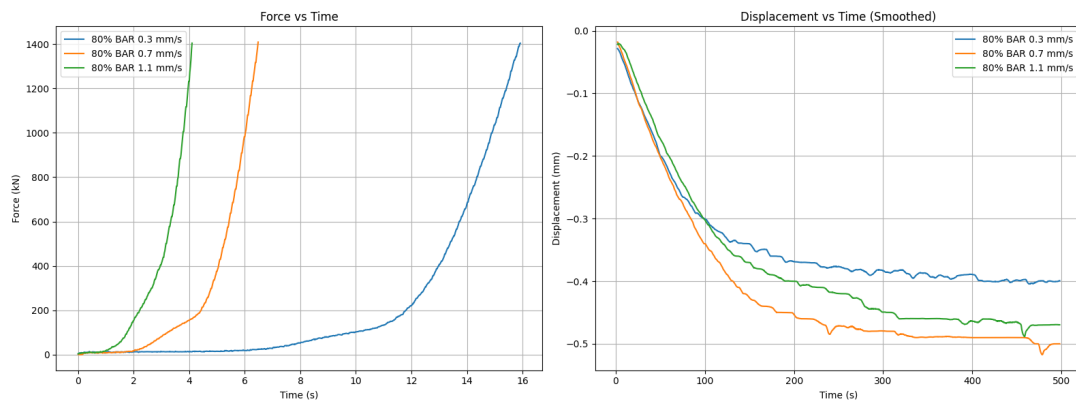


**Figure 4.3:** Force–time (left) and displacement–time (right) for 80 % CENTER charge at three closing speeds (0.3, 0.7, 1.1 mm/s).

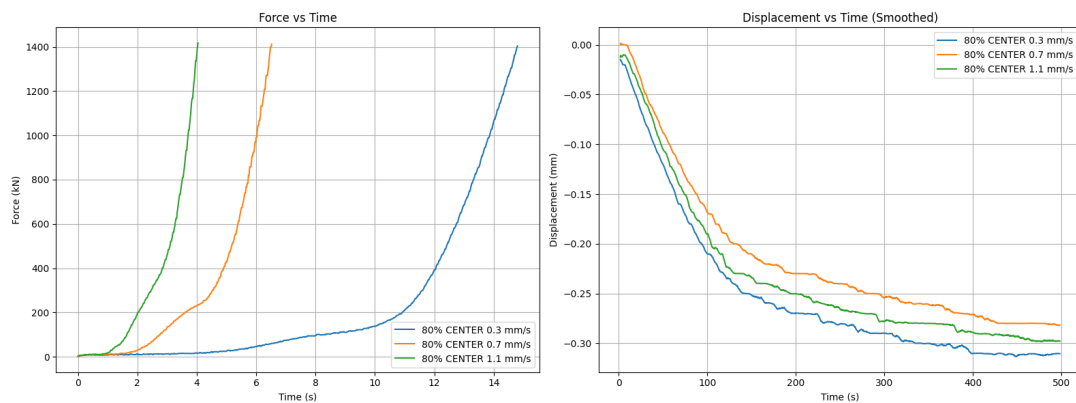


**Figure 4.4:** Force–time (left) and displacement–time (right) for 60 % BAR charge at three closing speeds (0.3, 0.7, 1.1 mm/s).

In order to determine the point at which the mold cavity was considered filled during compression, the measured displacement-time data were analyzed together with reference lines corresponding to the cavity thickness. At the beginning of each experiment, the measured displacement of the press corresponded to the initial charge thickness of 8 mm, representing the stacked SMC sheets placed in the mold. During compression, the material flowed outward while the press continued to close.

To estimate the thickness values at which the cavity was considered filled, the assumption of material incompressibility was initially made. Under this assumption, the initial charge volume—based on an 8 mm stack and the covered mold area—was equated to the mold cavity volume at full coverage. This yielded flow-stop thicknesses of 4.8 mm for the 60% coverage cases and 6.39 mm for the 80% coverage cases

## 4 Results and Discussion

$$A_{\text{cov}} h_{\text{init}} = A_{\text{mold}} h_{\text{flow}} \Rightarrow h_{\text{flow}} = \frac{A_{\text{cov}}}{A_{\text{mold}}} h_{\text{init}} \quad (4.1)$$

These values were used as reference lines in the displacement-time plots to identify the time at which in-plane flow was assumed to be completed. For example, in Figure 4.6, the intersection of the displacement curve with the 4.8 mm reference line indicates that the flow process was completed 10.380 seconds after the initial contact.

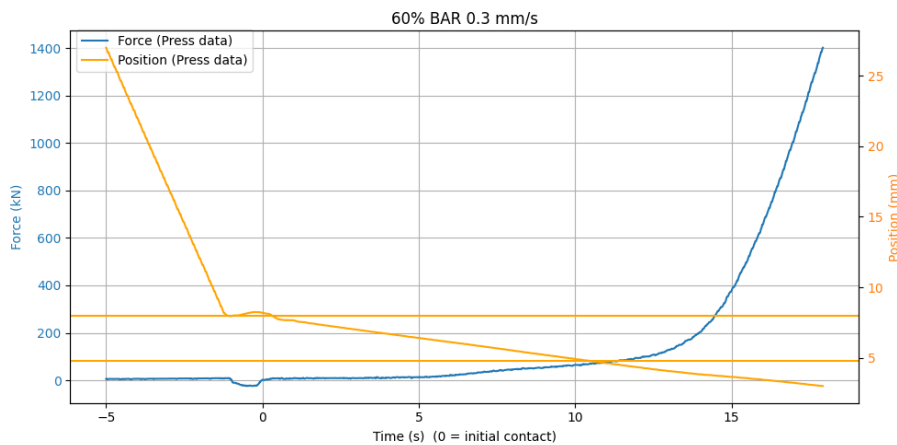


**Figure 4.5:** Force–displacement vs. time curves of the 60% configuration with reference lines.

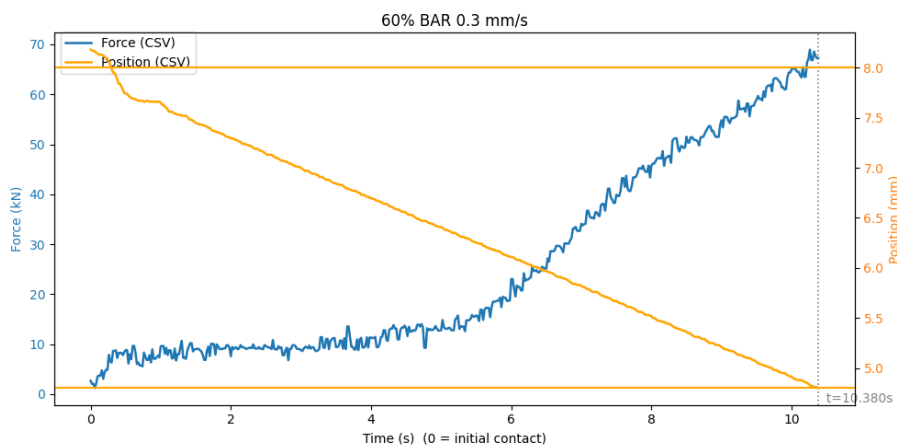


**Figure 4.6:** Force–displacement vs. time curves of the 60% configuration with reference lines, focused on the filling timeline.

This intersection time was then used as the cutoff point for further analysis of the experimental force–time curves, restricting evaluation to the interval from initial contact

up to the point of assumed flow completion. This was necessary because Moldflow does not simulate overfilling of the cavity.

However, subsequent weighing of the demolded parts revealed that the actual overfill (flashes and spillage) was minimal (Table 4.1 and Figure 4.7). This finding indicated that the incompressibility assumption was not valid: the additional press displacement observed in the displacement-time curves (Figures 4.1–4.4) cannot be explained by overfilling alone. Instead, a significant fraction of the displacement must be attributed to material compressibility and fiber packing during the compaction phase.

**Table 4.1:** SMC charge weight before and after compression, and calculated overfill percentage.

<b>Configuration</b>	<b>Initial weight [g]</b>	<b>Final weight [g]</b>	<b>Overfill [%]</b>
60% Center charge 0.3 mm/s	396	369	6.8
60% Center charge 0.7 mm/s	398	373	6.2
60% Center charge 1.1 mm/s	393	369	5.6
60% Bar charge 0.3 mm/s	388	360	7.2
60% Bar charge 0.7 mm/s	384	367	4.42
60% Bar charge 1.1 mm/s	414	388	4.2
80% Center charge 0.3 mm/s	542	512	5.5
80% Center charge 0.7 mm/s	527	501	4.9
80% Center charge 1.1 mm/s	543	515	5.1
80% Bar charge 0.3 mm/s	508	476	6.3
80% Bar charge 0.7 mm/s	525	480	8.5
80% Bar charge 1.1 mm/s	531	489	7.9

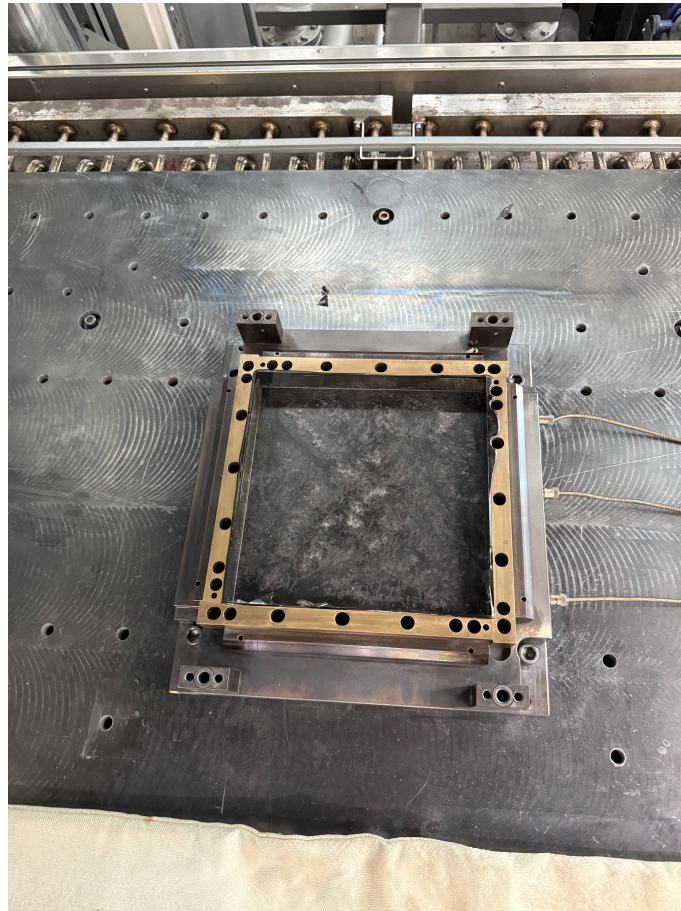


Figure 4.7: Picture of the SMC product after demolding.

### 4.2 Verification of Optimization in 2D Case

Before extending the optimization to the full set of rheological parameters, the functionality of the optimization loop was verified using a simplified case with two parameters: the wall slip parameters  $\tau_w$  and  $m$ . This test case was chosen because wall slip strongly influences the press force response in compression molding, while at the same time reducing the dimensionality of the search space, making it an ideal scenario for initial validation. The BO loop was implemented with a GP surrogate model and the LogEI acquisition function. An initial design of experiments was generated using LHS, followed by iterative evaluations in which new candidate points were proposed and tested through Moldflow simulations.

A Moldflow simulation was first carried out with selected parameters, and the resulting force–time curve was designated as the “real” or master curve. Subsequently, five simulations were conducted with parameter sets generated by LHS in order to build the initial surrogate model. This setup offered two advantages. First, it established a

controlled environment in which the ground truth was known, allowing the correctness of the pipeline to be verified. Second, it enabled visual exploration of the parameter space, since the problem was limited to two dimensions. An interactive contour plot of the loss function was generated, showing that the optimizer traversed the parameter space from the Latin hypercube initial samples toward the true parameter values. The optimization trajectory clearly converged toward the region around the ground truth, confirming that the Gaussian process surrogate model and acquisition function were working as intended. This restriction to two parameters was chosen because higher-dimensional parameter spaces (e.g., including viscosity parameters) cannot be directly visualized without projection, whereas the two-dimensional case allows for straightforward graphical representation. The ground truth (blue point) was chosen to lie inside the search space. Figures 4.8–4.10 show the GP model with uncertainty for the initial sampling, viewed from different angles. The red point represents the next suggested candidate, while black dots denote the training samples and the blue dot indicates the ground truth. The subsequent optimization process is illustrated step by step in Figures 4.11–4.13, where the surrogate model is progressively refined as new candidate points are evaluated. While this proof-of-concept case used synthetic data, it demonstrated that the pipeline was able to recover the correct slip parameters when the true solution was embedded in the model. In the subsequent sections, the same framework is applied to experimental data, where the ground truth is not known and the optimization instead seeks parameters that best reproduce the measured press curves.

Before optimization, simulations with randomly chosen parameter values deviated strongly from the “real” curve (i.e., the curve generated with known rheological parameters). In particular, the peak force levels and the slope of the loading phase were poorly matched. These “guess vs. real” plots established the baseline error that motivated the use of the GP model and the optimization process.

After optimization, the force–time curves aligned much more closely with the “real” data. Both the overall shape of the curves and the peak forces were reproduced with higher accuracy. The improvement was particularly evident when plotting the real and optimized curves together, showing a substantial reduction in MSE. Together, these visualizations provided insights as well as verification for both the optimization loop and the automation pipeline. The 3D loss landscape revealed the structure of

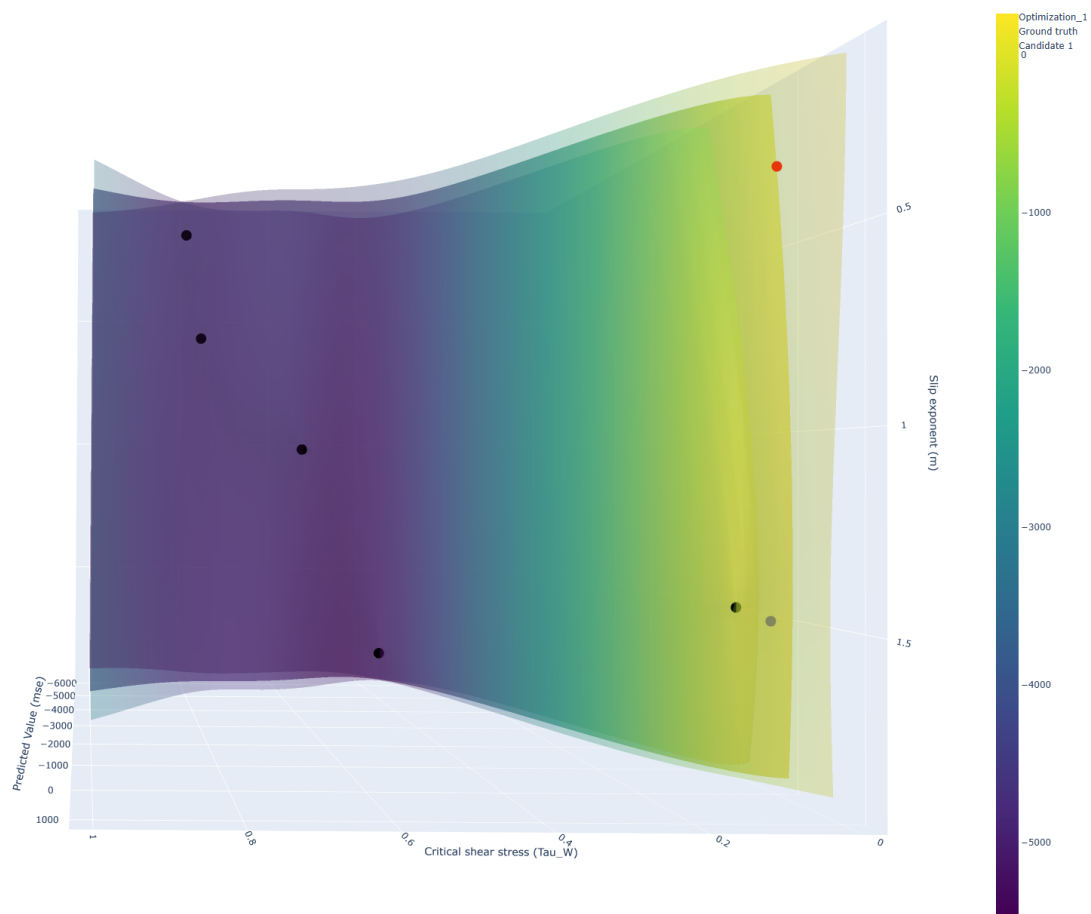


**Figure 4.8:** 3D loss landscape, top view. Black dots: training parameters, red dot: candidate parameter, blue dot: ground truth.

the parameter space and the ability of BO to converge, while the force–time curves confirmed the effectiveness of the identified parameters.

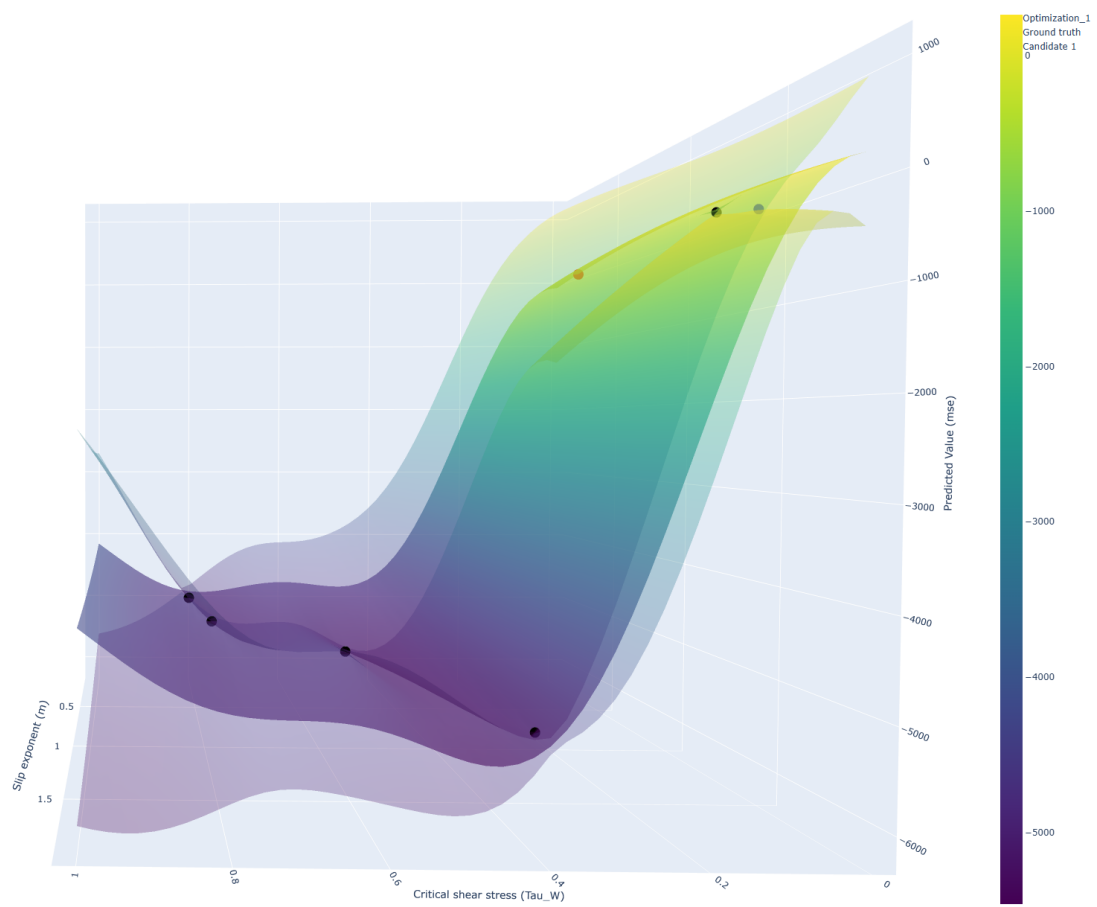


**Figure 4.9:** 3D loss landscape, side view. Black dots: training parameters, red dot: candidate parameter, blue dot: ground truth.

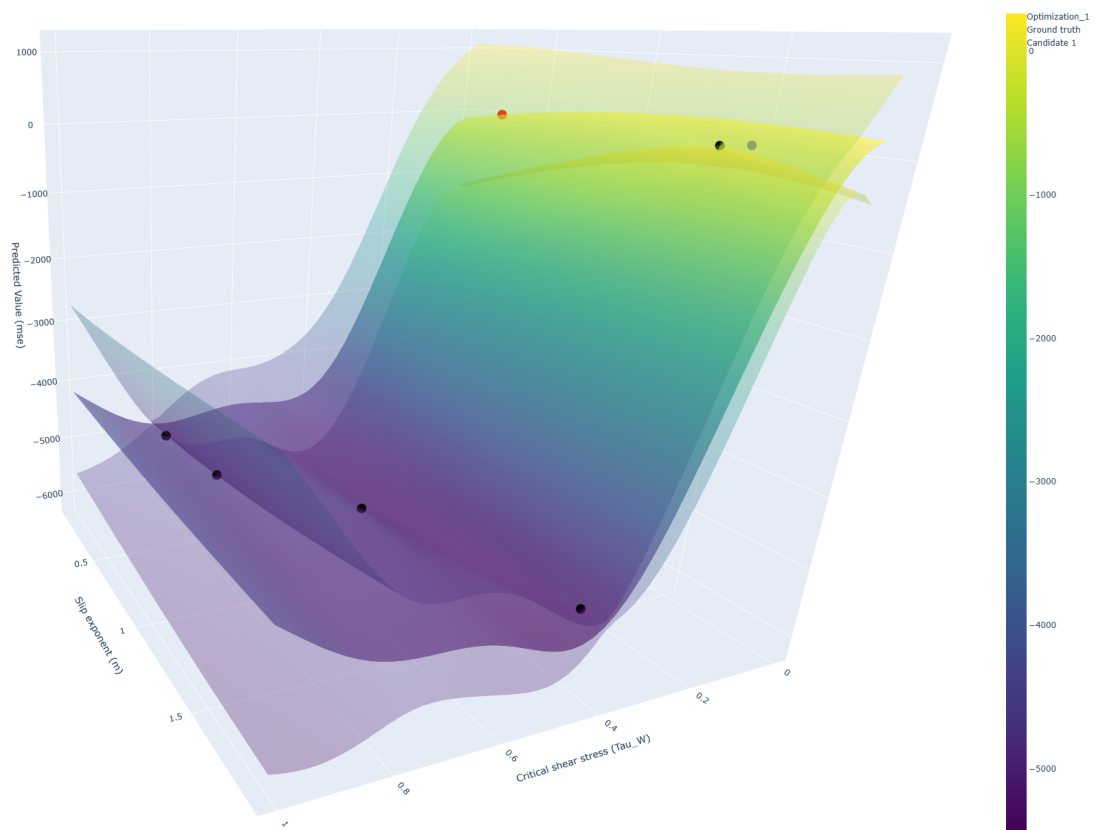


**Figure 4.10:** 3D loss landscape, perspective view. Black dots: training parameters, red dot: candidate parameter, blue dot: ground truth.

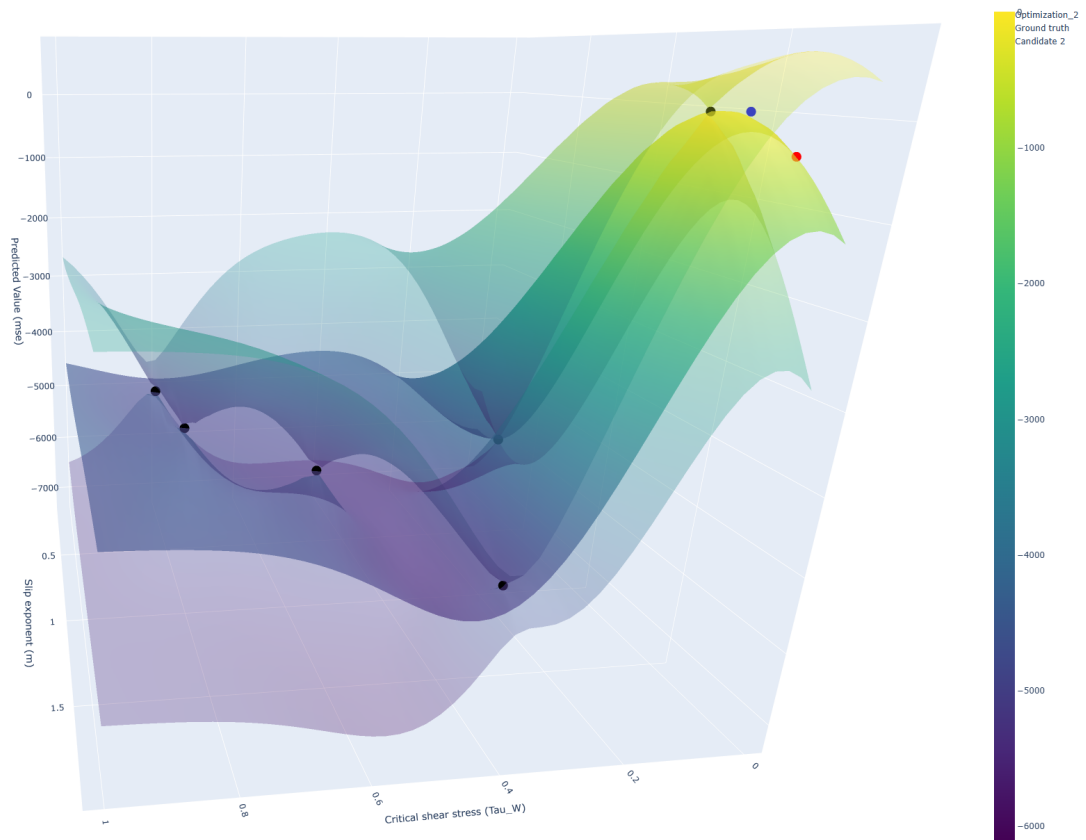


**Figure 4.11:** Optimization step 1: initial sampling with LHS and GP surrogate model.

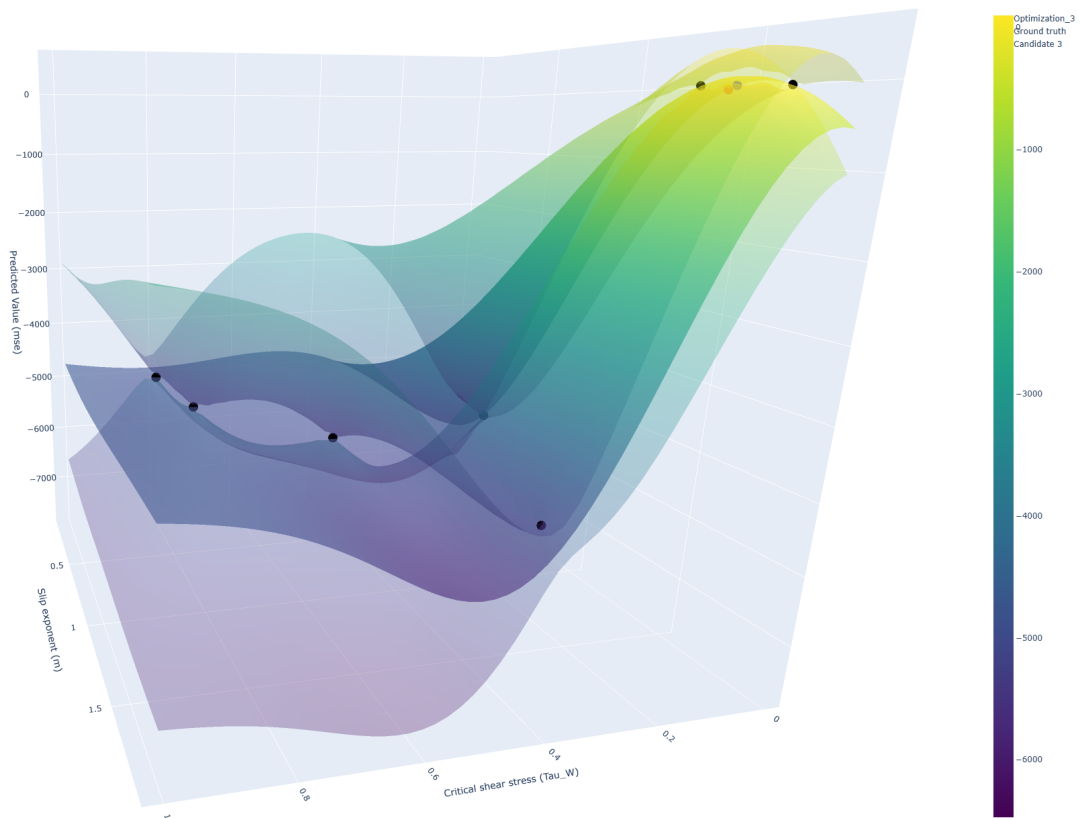


**Figure 4.12:** Optimization step 2: updated surrogate model and candidate selection.

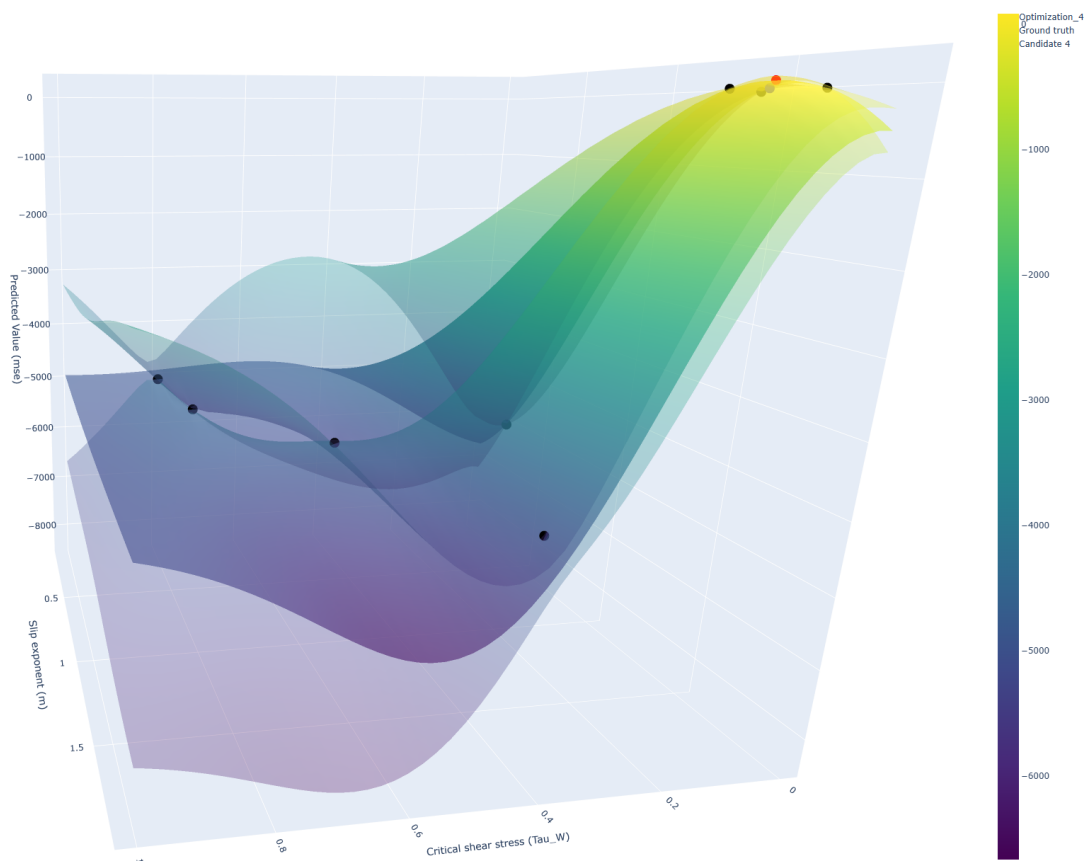
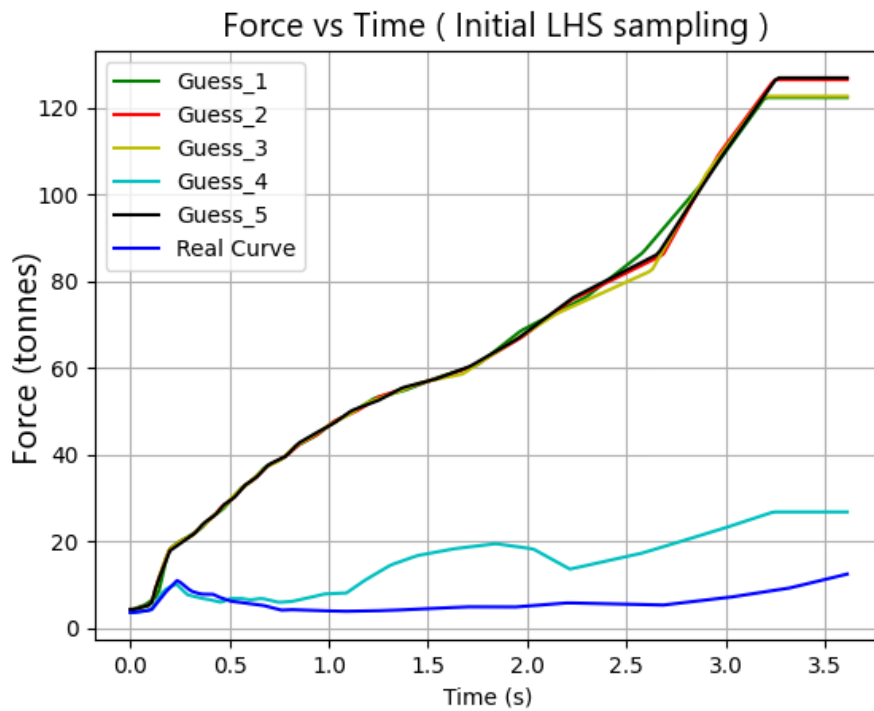
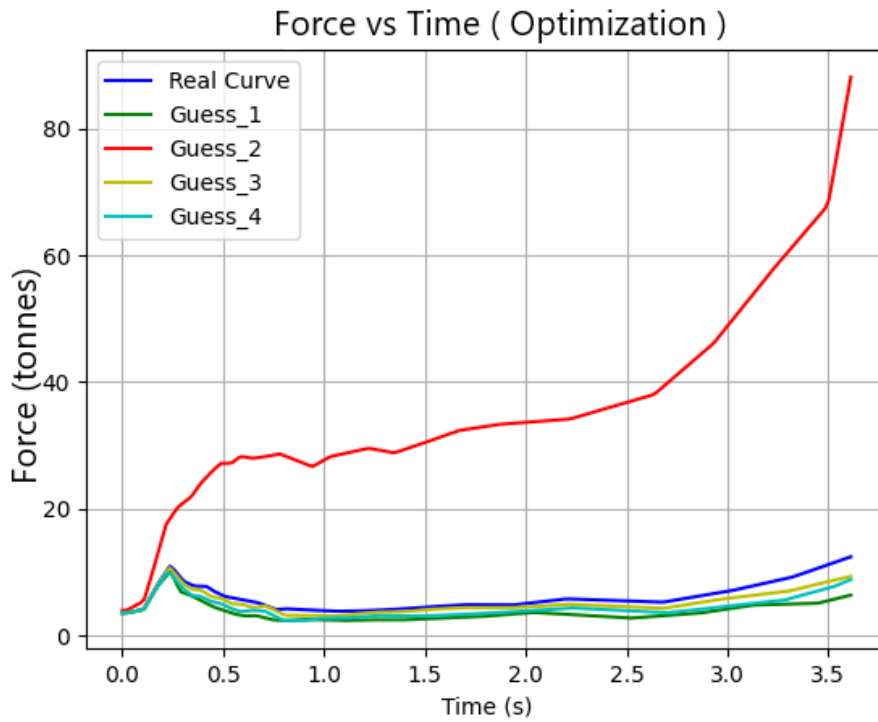


Figure 4.13: Optimization step 3: further refinement of the surrogate model.



**Figure 4.14:** Force–time curves from simulations using initial guess parameters compared to "real" curve. Substantial deviations motivate optimization.



**Figure 4.15:** Force–time curves after optimization compared to "real" curve.

### 4.3 Model Training

The GP model training was initialized with the generation of 30 initial parameter sets using LHS. This method divides each parameter range into equal intervals and selects random points, providing a balanced representation across the five-dimensional space [50]. For the nine training configurations—variations in mold geometry, charge placement, and processing conditions—Autodesk Moldflow simulations were conducted, each requiring approximately 20 minutes, to produce force–time and displacement–time curves. This resulted in a total of 270 initial data points, linking parameter sets to error metrics calculated as the mean squared error (MSE) between simulated and experimental master curves.

The error data fed into the GP model was aggregated using the loss function in (3.7), where  $p = 9$  represents the number of configurations,  $\psi$  denotes the parameter vector, and  $w_F$  and  $w_D$  are weights adjusted for full processes under speed control ( $w_F = 1$  and  $w_D = 0$ ). The GP model was trained using an Radial Basis Function (RBF) kernel with a noise term to account for uncertainties. Initial training curves for one configuration and for all configurations are shown in Figures 4.16 and 4.19.

Because Moldflow assumes the material to be incompressible, the simulated flow times were shorter than in real experiments. In reality, press displacement continues beyond the flow-stop thicknesses due to compressibility and fiber packing, but Moldflow terminates the flow once the cavity is filled. If the prescribed cavity thickness is set exactly to the calculated flow-stop values (4.8 mm for 60% coverage and 6.39 mm for 80% coverage), the simulation ends too early and may result in numerical errors. To avoid this, the CAD model was adjusted by slightly increasing the cavity thickness beyond the calculated values. This ensured that Moldflow simulations ran smoothly and captured the complete flow process up to cavity filling, without producing errors from prematurely truncated runs.

The duration of the fill time in simulations plays a critical role in enhancing the quality and robustness of the GP surrogate model. Longer fill times, which provide a greater number of data points over the simulation period, yield a richer dataset for training the GP, thereby improving its predictive accuracy and uncertainty estimation.

Binois et al. demonstrated that adding more runs—either as new points or replicates—improves the global accuracy of GP surrogates [51]. A similar conclusion was reached by Kimpton et al., who explicitly noted that accuracy depends strongly on the number and placement of design points, and that additional points improve the

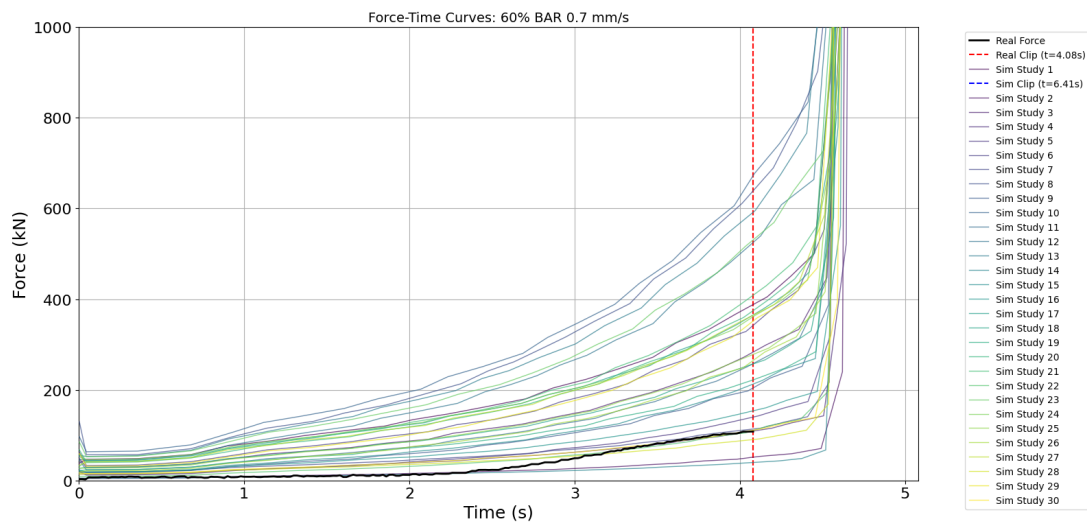


**Figure 4.16:** Resulting force–time curves of training data compared to the master curve for the 60% BAR 0.7 mm/s configuration. “Real Force” represents the master curve, and the 30 Sim Study curves are the training curves from 30 generated parameter sets. “Real Clip” indicates the point where the master and training curves are clipped according to the mold filling assumption.

predictive power of the GP [52]. Longer fill times allow for extended observation of the force–time curves across the nine configurations, generating a higher density of data points. This increased temporal resolution is beneficial for capturing the behavior of the SMC material. For the GP model, which relies on a covariance structure to interpolate between observed points, a larger and more diverse dataset reduces overfitting and enhances the model’s ability to generalize across the parameter space.

It was observed that 80% charges filled more quickly than 60% charges, resulting in a difference in data richness. With increased closing speeds, fill times were further reduced. Combinations of 80% charges and the highest velocity configurations therefore yielded poorer training data compared to 60% charges and slower configurations. The contrast between the 60% BAR 0.3 mm/s configuration and the 80% BAR 1.1 mm/s configuration can be seen in Figures 4.17 and 4.18. Future work could explore experimental setups designed to yield longer fill times.

## 4 Results and Discussion

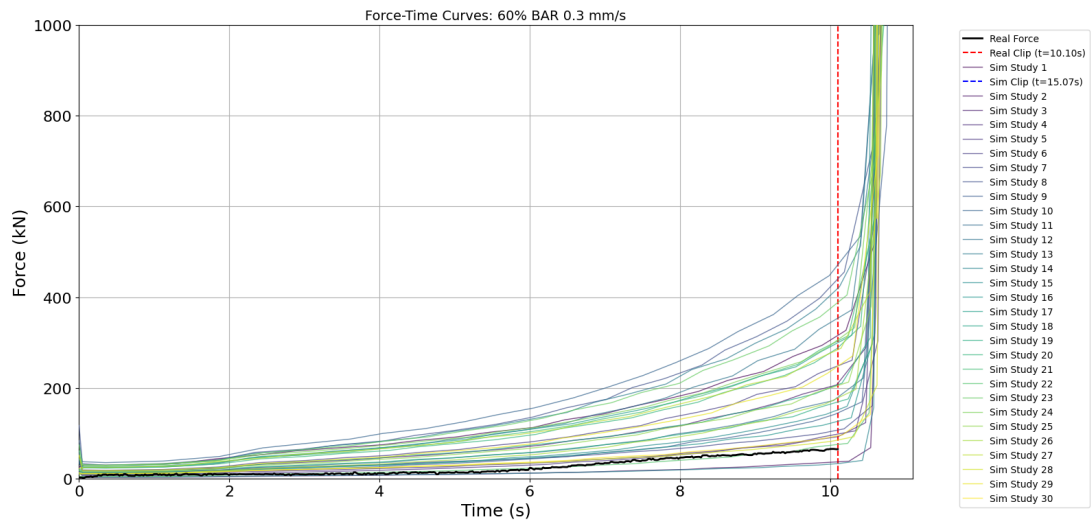


Figure 4.17: Force-time curves for training and real curves for 60 BAR 0.3 mm/s configuration.

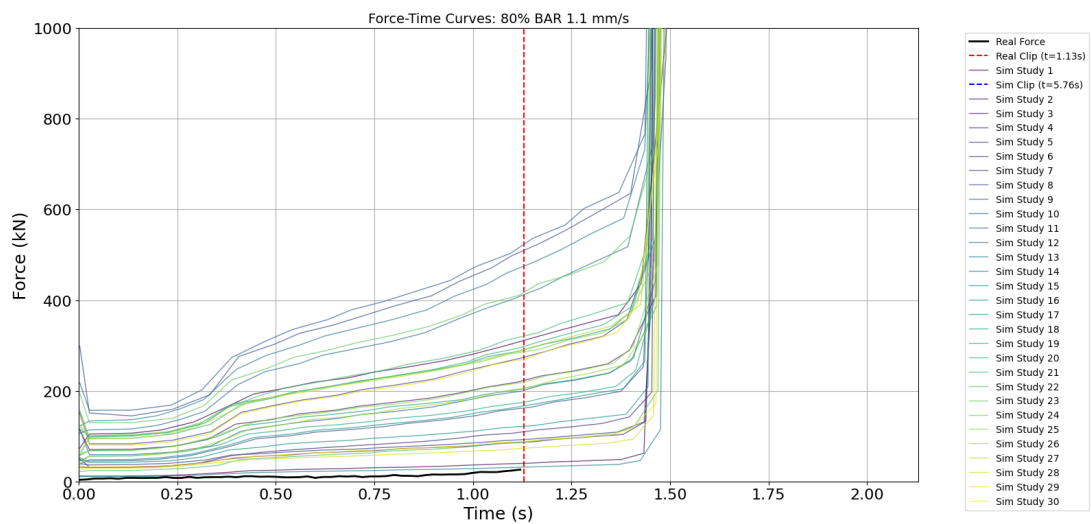


Figure 4.18: Force-time curves for training and real curves for 80 BAR 1.1 mm/s configuration.

## 4 Results and Discussion

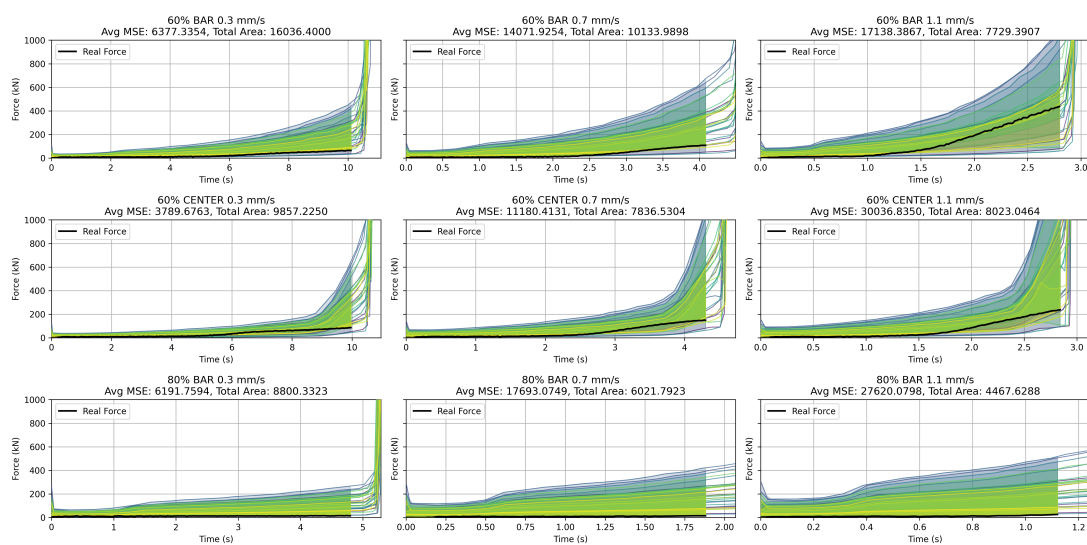


Figure 4.19: 3x3 subplot grid of all training configurations.

## 4.4 Optimization

The optimization iterated over 15 runs, with each cycle involving: (1) the GP predicting expected loss and uncertainty, (2) logEI selecting the next candidate balancing exploration and exploitation, (3) Moldflow simulations with new parameter set and (4) updating the GP with the new summed MSE values. This workflow was automated via a Python script and repeated until the 15-run budget was exhausted. The optimization was carried out in a bounded five-dimensional parameter space, consisting of three viscosity parameters ( $n, \tau^*, B$ ) from the modified Cross model and two wall-slip parameters ( $\tau_w, m$ ) from the Moldflow slip-velocity formulation. The parameter bounds were chosen to reflect the physically reasonable range of SMC behavior reported in the literature, while still enabling the optimizer to explore meaningful variability [53–55]:

$$n \in [0.2, 0.6]$$

$$\tau^* \in [10^3, 10^5] \text{ Pa}$$

$$B \in [10^3, 10^5] \text{ Pa}$$

$$\tau_w \in [0.005, 1.0] \text{ MPa}$$

$$m \in [1.0, 1.9]$$

These ranges were guided by earlier rheological characterizations of SMC and related compression molding compounds, which consistently report shear-thinning flow with power-law exponents in the range of 0.2–0.6 and critical shear stresses on the order of  $10^3$ – $10^5$  Pa [6, 19]. The lower and upper limits for the wall-slip parameters were selected based on experimental observations that SMC exhibits substantial slip at the mold wall, with slip coefficients typically between  $5 \cdot 10^{-3}$  and 1 MPa. These values were tested beforehand to ensure numerical stability of the simulations.

The viscosity behavior within the parameter bounds is illustrated in Figure 4.20, showing the predicted viscosity–shear rate curves for the lower and upper bounds.

Further confirmation of the wall-slip effect is provided by the cross-section velocity profile shown in Figure 4.21. The diagram reveals that the velocity of the material is significantly higher in regions close to the mold walls, while the bulk of the material in the central region moves more slowly. This velocity gradient across the thickness is characteristic of slip-dominated flow, as opposed to a no-slip condition where veloc-

## 4 Results and Discussion

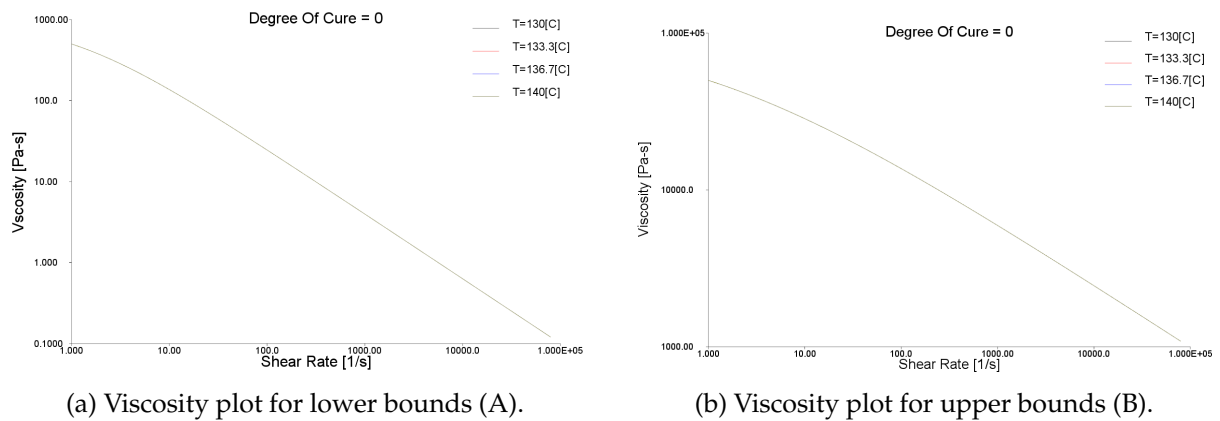


**Figure 4.20:** Viscosity profiles for lower and upper bounds of the parameter space.

ity would drop to zero at the wall. The observation is consistent with experimental studies reporting that SMC charges undergo slip at the mold surface rather than adhering completely, and supports the choice of including wall-slip parameters in the optimization.

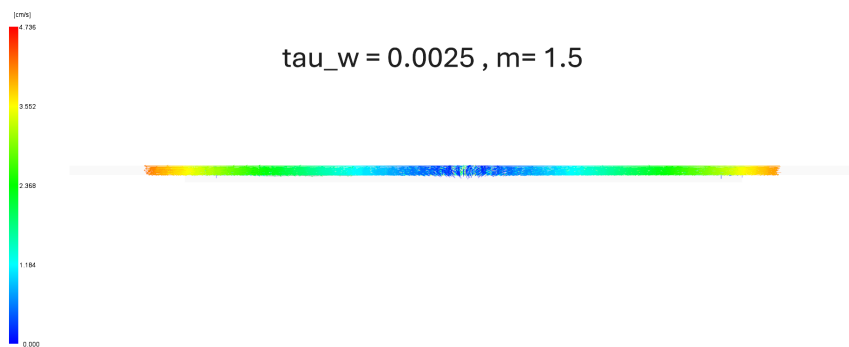


**Figure 4.21:** Cross-section velocity profile of the compression simulation. High velocities near the mold walls and reduced velocities in the bulk confirm slip-dominated flow behavior.

Constraining the parameter space in this way serves two purposes. First, it prevents the optimizer from exploring non-physical regions that would produce meaningless simulations. Second, it reduces the risk of non-unique solutions, which is a common issue in inverse identification problems where different parameter combinations can reproduce the same macroscopic curve. By restricting the optimization to a literature-supported domain, the identified parameters remain both interpretable and consistent with established SMC rheology. The summed MSE, calculated as the average of the nine-configuration-specific MSEs, serves as the primary metric for comparing the optimization runs (Figure 4.2).

Optimization Run	MSE Value
1	30660.53
2	48317.80
3	36277.84
4	36161.50
5	158392.27
6	33916.62
7	25607.72
8	48272.46
9	38901.57
10	18702.30
11	20926.71
12	18384.70
13	25985.49
14	28364.18
15	48001.68

**Table 4.2:** Optimization runs with respective MSE values.

The sequence shows a non-monotonic reduction, with the lowest summed MSE reached at Optimization 12, corresponding to a 40.1% reduction from Optimization 1. However, the process includes significant fluctuations: Optimization 5 and Optimization 15 represent peaks, suggesting that the LogEI function’s balance between exploration and exploitation occasionally directed the search toward high-error regions. Overall, the optimization achieved an improvement of the best observed MSE value over 15 iterations (Figure 4.22).

In Run 1, the initial candidate parameters resulted in a summed MSE of 30,660. The 3×3 visualization illustrated the variability in the simulated force–time curves compared to the experimental curves, with error regions highlighted. The 60% BAR 1.1 mm/s and 60% CENTER 1.1 mm/s configurations exhibited significantly higher MSE values than the other configurations, while the 80% configurations yielded the lowest errors.

By Run 7, optimization had reduced the previously high MSE values from these configurations. The 60% BAR 1.1 mm/s configuration improved by 63%, and the 60% CENTER 1.1 mm/s configuration by 77%. In contrast, the errors for the 80% configurations increased drastically, by approximately 2500%. Nevertheless, the summed MSE improved overall compared to Optimization 1. The variance across configurations suggests that certain configurations may influence the training set more strongly than others.

The performance of Run 12 relative to Run 1 shows improvements particularly for the 80% BAR configurations. Combined with minor improvements in most of the 60% BAR

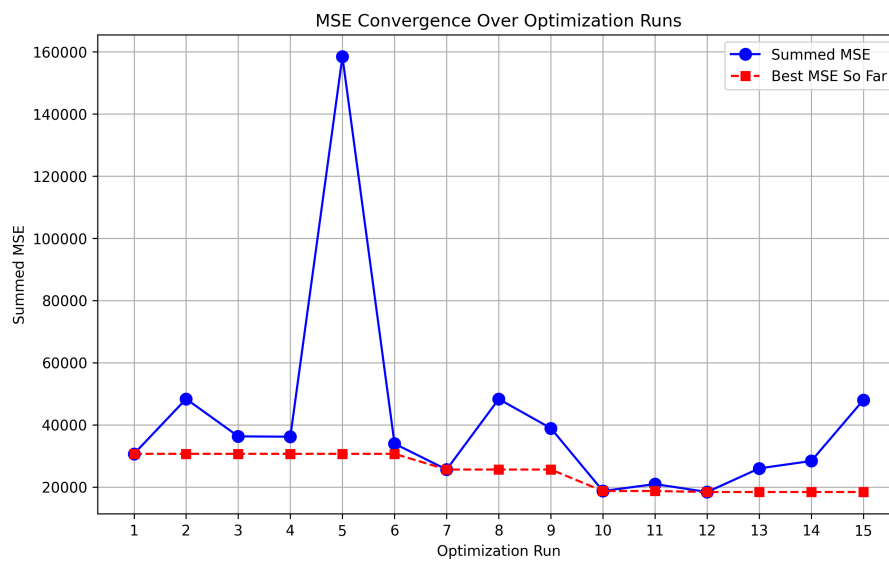


**Figure 4.22:** MSE convergence plot.

and 60% CENTER configurations, this resulted in the overall best optimization outcome. However, improvements across configurations were inconsistent, as can be seen in the plots. Even though the degree of improvement varied, the overall progress of the model within the given optimization runs is evident.

## 4 Results and Discussion

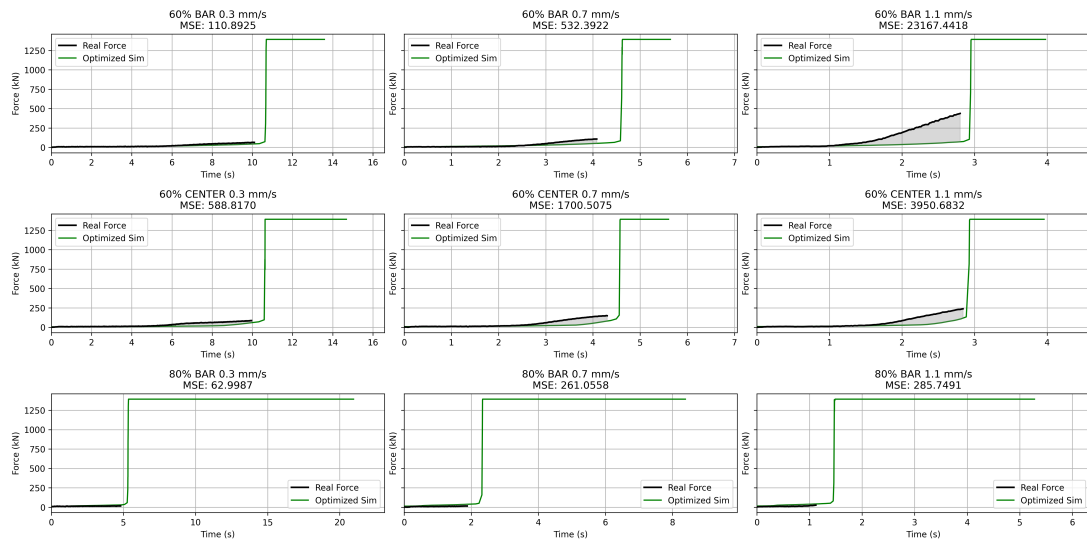


Figure 4.23: Optimization 1 across all configurations.

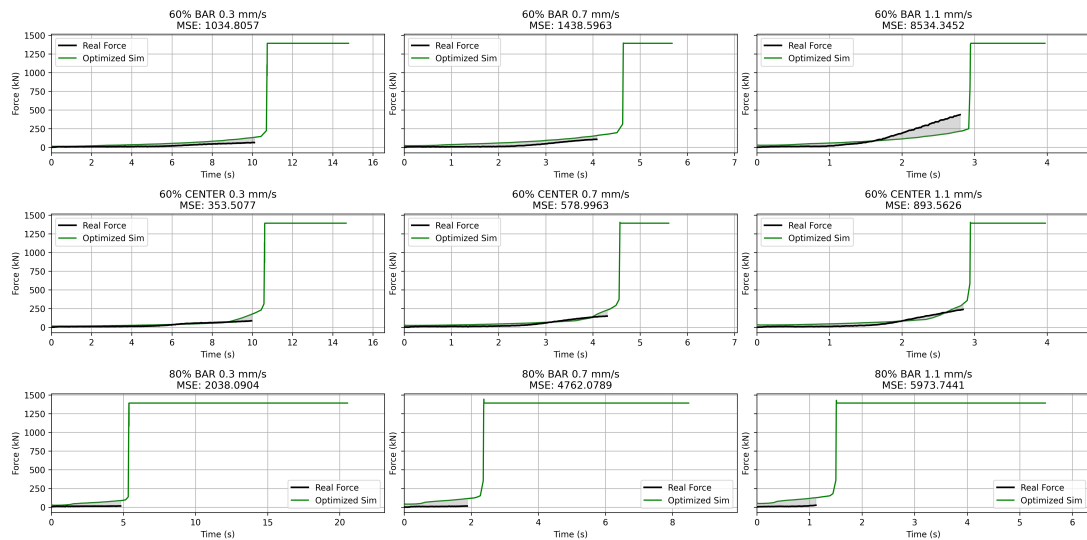


Figure 4.24: Optimization 7 across all configurations.

## 4 Results and Discussion

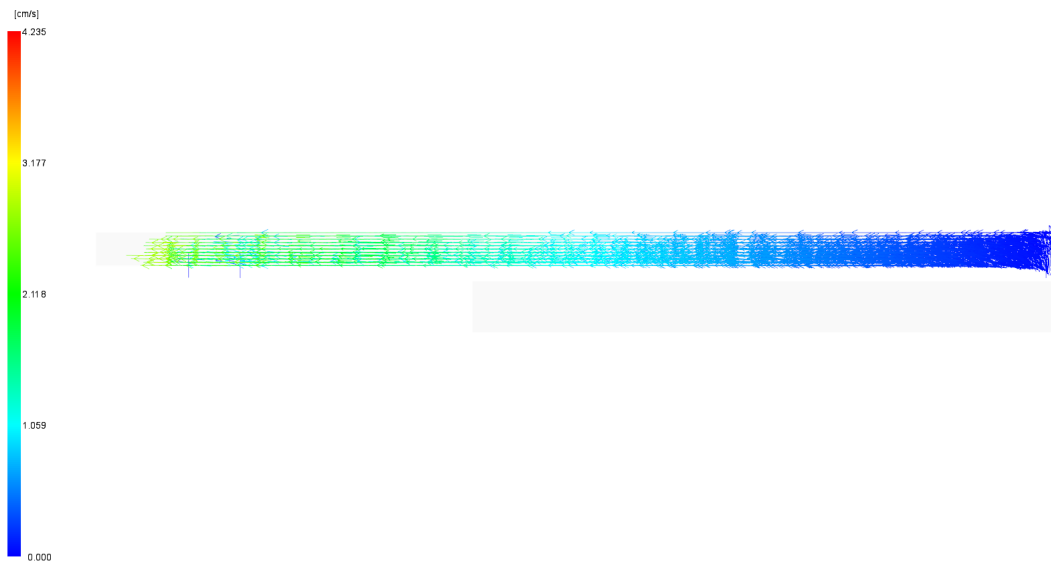


Figure 4.25: 60% BAR 0.7 mm/s configuration's speed profile at the 4th second of the flow.

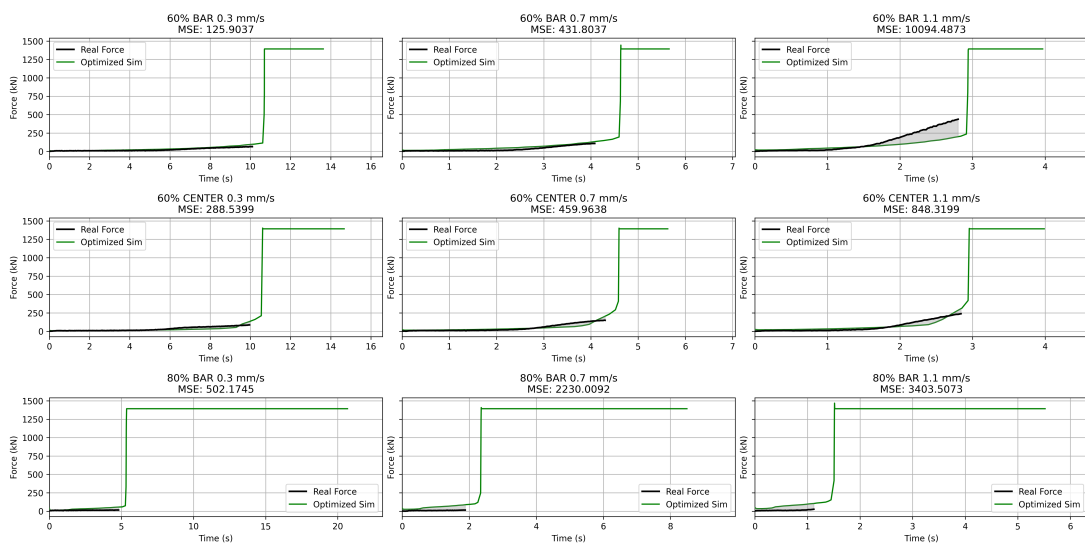


Figure 4.26: Optimization 12 across all configurations.

### 4.5 Validation

To evaluate the predictive capability of the model, a validation study was carried out using independent press trials. Three configurations, not included in the GP training set, were selected. Each configuration corresponded to an 80% CENTER configuration at three different speeds, as previously described in Section 3.1.

The optimized parameter set was then used in Moldflow simulations of the validation configurations. The resulting force–time curves were directly compared with their experimental counterparts. Figure 4.27 shows the comparisons for the three validation cases. Across all cases, the optimized parameters reflect the overall shape of the experimental force–time response, but the quantitative agreement is weak. Among the three cases, the 0.3 mm/s configuration showed the poorest agreement, while the 0.7 mm/s and 1.1 mm/s cases were captured more accurately. The discrepancy at 0.3 mm/s is primarily caused by a force peak near the end of the filling phase, which is also visible in some of the training data.

This discrepancy arises from two sources: (1) Moldflow’s assumption of incompressibility, which causes the simulated filling time to differ from the actual filling time observed in experiments, and (2) the modifications applied to the CAD model to compensate for overfilling. These adjustments, while necessary to avoid numerical errors in Moldflow, introduce differences in the later stages of the force–time curves. Nevertheless, in the earlier stages of the curves—up to cavity filling—the simulated and experimental curves show smaller deviations.

Overall, the optimized parameter set was able to predict the force response of the validation cases with acceptable accuracy, despite deviations. These deviations can be attributed to the assumptions of incompressibility, the quality of the training data (limited by short filling times), and the modifications made to the simulation model for compensating overfill.

## 4 Results and Discussion

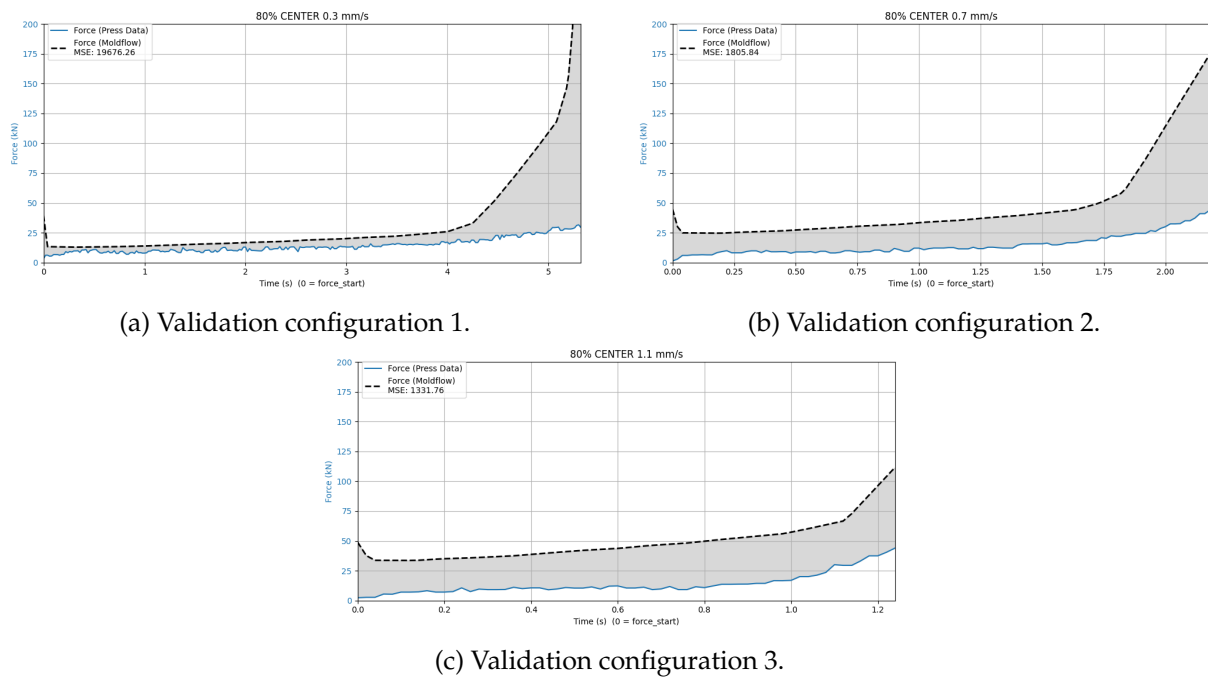


**Figure 4.27:** Comparison of experimental and simulated force–time curves for three validation configurations.

### 4.6 Comparison with Literature

The present work developed a data-driven framework for identifying rheological parameters in the compression molding of SMCs. A GP surrogate was employed within a BO loop to iteratively calibrate a modified Cross viscosity model and a slip-velocity model against experimental press curves. Unlike conventional rheometry-based characterization, this method directly incorporates in-mold process data, thereby accounting for industrial conditions such as fiber–matrix interactions, lubrication layers, and complex flow patterns. In this section, the results are compared with related approaches in the literature, highlighting similarities, differences, and the novel contributions of this work.

This thesis explicitly considers SMC as a non-Newtonian and anisotropic material, consistent with experimental observations of shear thinning and fiber-induced anisotropy reported in earlier rheological studies. By calibrating the Cross viscosity model and the slip law, the framework captures not only flow resistance but also wall–charge interactions that strongly influence the flow. Nevertheless, the approach still lacks the complete physics of the process, since the compressibility of the material has not been accounted for in the simulations.

Miranda-Valdez et al. recently applied BO to infer viscoelastic models from oscillatory, creep, and relaxation experiments. Their results showed that BO can efficiently navigate highly non-convex parameter landscapes, avoiding local minima that often trap gradient-based routines [56]. The methodology presented in this thesis closely aligns with theirs in terms of the optimization framework but differs in application domain and material modeling. Moreover, while their study fitted rheological data obtained under controlled laboratory conditions, this thesis calibrates results obtained from an industrial-scale press machine.

Research by Ferré Sentis et al. and Hohberg et al. underlines that compressibility is an intrinsic property of SMCs, driven by both pore dynamics and rheological effects. While the present thesis focuses on identifying non-Newtonian viscosity and slip parameters, it acknowledges that compressibility remains a crucial factor for achieving fully predictive simulations. The Bayesian optimization framework developed here could be extended in future work to include compressibility parameters, potentially combining insights from the aforementioned studies. This would enable a more comprehensive description of SMC behavior within a unified optimization framework.

## 5 Conclusions

The objective of this thesis is to identify rheological parameters for SMC compression molding using a data-driven approach. Traditional rheometers are limited in capturing the combined effects of anisotropic viscosity and wall slip, while modern in-situ rheometers, though more representative, remain complex and resource-intensive. Developments in machine learning algorithms over the years have paved the way for interdisciplinary studies within materials science. These factors motivated this thesis to establish a preliminary methodology for the inverse characterization of rheological parameters of SMCs. To achieve this, an automation pipeline was established that coupled Autodesk Moldflow simulations with a Python-based optimization framework.

The results demonstrated that BO provides an efficient approach for parameter identification. After 15 optimization runs, the error between the experimental master curves and the simulation results was reduced. The optimization showed the distinctive behavior of balancing exploration and exploitation through the acquisition function. While the effects of pores and compressibility were not included in the present optimization framework, the results demonstrate that the methodology can be extended to include such phenomena in the future. Combining rheological calibration with compressibility modeling represents a promising direction for developing data-driven inverse material characterization.

A key step in verifying the methodology was the proof-of-concept study using synthetic results. In this study, the optimization loop was tested on a simplified two-parameter slip model with known ground-truth values. The Gaussian process surrogate model and acquisition function successfully converged toward the correct parameters, demonstrating that the pipeline was able to recover hidden material properties when the true solution was embedded in the model. This synthetic validation provided confidence in the reliability of the framework before applying it to experimental press data, where the ground truth is unknown.

## 5 Conclusions

---

Future work should focus on expanding the methodology to include compressibility effects and exploring new configuration setups to enhance model training. Ultimately, embedding such physical descriptions into the developed pipeline offers a pathway toward increasing the predictive capability of virtual process chains in composite manufacturing.

# Bibliography

- [1] L. Orgéas and P. Dumont, "Sheet Molding Compounds," in *Wiley Encyclopedia of Composites*, 2012, pp. 2683–2718. DOI: [10.1002/9781118097298.weoc222](https://doi.org/10.1002/9781118097298.weoc222).
- [2] T. Osswald and N. Rudolph, "6 - Rheometry," in *Polymer Rheology*, T. Osswald and N. Rudolph, Eds., Hanser, 2015, pp. 187–220. DOI: <https://doi.org/10.3139/9781569905234.006>.
- [3] L. J. Lee, L. F. Marker, and R. M. Griffith, "The rheology and mold flow of polyester sheet molding compound," *Polymer Composites*, vol. 2, no. 4, pp. 209–218, 1981. DOI: <https://doi.org/10.1002/pc.750020412>. eprint: <https://4spepublications.onlinelibrary.wiley.com/doi/pdf/10.1002/pc.750020412>.
- [4] M. R. Barone and D. A. Caulk, "Kinematics of flow in sheet molding compounds," *Polymer Composites*, vol. 6, no. 2, pp. 105–109, 1985. DOI: <https://doi.org/10.1002/pc.750060208>. eprint: <https://4spepublications.onlinelibrary.wiley.com/doi/pdf/10.1002/pc.750060208>.
- [5] P. Dumont, L. Orgéas, D. Favier, P. Pizette, and C. Venet, "Compression moulding of SMC: In situ experiments, modelling and simulation," *Composites Part A: Applied Science and Manufacturing*, vol. 38, no. 2, pp. 353–368, 2007. DOI: <https://doi.org/10.1016/j.compositesa.2006.03.010>.
- [6] S. Le Corre, L. Orgéas, D. Favier, A. Tourabi, A. Maazouz, and C. Venet, "Shear and compression behaviour of sheet moulding compounds," *Composites Science and Technology*, vol. 62, no. 4, pp. 571–577, 2002. DOI: [https://doi.org/10.1016/S0266-3538\(01\)00151-8](https://doi.org/10.1016/S0266-3538(01)00151-8).
- [7] P. Dumont, L. Orgéas, S. Le Corre, and D. Favier, "Anisotropic viscous behavior of sheet molding compounds (SMC) during compression molding," *International*

- Journal of Plasticity*, vol. 19, no. 5, pp. 625–646, 2003. DOI: [https://doi.org/10.1016/S0749-6419\(01\)00077-8](https://doi.org/10.1016/S0749-6419(01)00077-8).
- [8] O. Guiraud, P. Dumont, L. Orgéas, and D. Favier, “Rheometry of compression moulded fibre-reinforced polymer composites: Rheology, compressibility, and friction forces with mould surfaces,” *Composites Part A: Applied Science and Manufacturing*, vol. 43, no. 11, pp. 2107–2119, 2012. DOI: <https://doi.org/10.1016/j.compositesa.2012.06.006>.
- [9] M. Hohberg, L. Kärger, F. Henning, and A. Hrymak, “Rheological measurements and rheological shell model Considering the compressible behavior of long fiber reinforced sheet molding compound (SMC),” *Composites Part A: Applied Science and Manufacturing*, vol. 95, pp. 110–117, 2017. DOI: <https://doi.org/10.1016/j.compositesa.2017.01.006>.
- [10] “Molding Compounds,” in *Composites*, ASM International, 2001. DOI: 10.31399/asm.hb.v21.a0003370. eprint: <https://dl.asminternational.org/handbooks/book/chapter-pdf/524825/a0003370.pdf>.
- [11] I. Swentek, “New epoxy systems enabling styrene-free high-performance SMC manufacturing,” in *JEC world: presentation*, Paris, France, 2017.
- [12] A. Kraemer, S. Lin, D. Brabandt, T. Böhlke, and G. Lanza, “Quality Control in the Production Process of SMC Lightweight Material,” *Procedia CIRP*, vol. 17, pp. 772–777, 2014, Variety Management in Manufacturing. DOI: <https://doi.org/10.1016/j.procir.2014.01.138>.
- [13] J. Gupta, N. Reynolds, T. Chiciudean, and K. Kendall, “A comparative study between epoxy and vinyl ester CF-SMC for high volume automotive composite crash structures,” *Composite Structures*, vol. 244, p. 112299, 2020. DOI: <https://doi.org/10.1016/j.compstruct.2020.112299>.
- [14] T. Rademacker, M. Fette, and G. Jüptner, “Nachhaltiger Einsatz von Carbonfasern dank CFK-Recycling,” *Lightweight Design*, vol. 11, no. 5, pp. 12–19, 2018. DOI: [10.1007/s35725-018-0046-7](https://doi.org/10.1007/s35725-018-0046-7).
- [15] T. Whelan and J. Goff, “Sheet molding compound,” in *Molding of Thermosetting Plastics*. Boston, MA: Springer US, 1990, pp. 75–85. DOI: [10.1007/978-1-4615-9759-9\\_10](https://doi.org/10.1007/978-1-4615-9759-9_10).

- [16] A. J. Imbsweiler, "Sheet Molding Compound processing: Characterization and numerical representation of the flow behavior," en, Ph.D. dissertation, Technische Universität München, 2025, p. 248.
- [17] M. Barone and D. Caulk, "The effect of deformation and thermoset cure on heat conduction in a chopped-fiber reinforced polyester during compression molding," *International Journal of Heat and Mass Transfer*, vol. 22, no. 7, pp. 1021–1032, 1979. DOI: [https://doi.org/10.1016/0017-9310\(79\)90175-3](https://doi.org/10.1016/0017-9310(79)90175-3).
- [18] R. J. Silva-Nieto, B. C. Fisher, and A. W. Birley, "Predicting mold flow for unsaturated polyester resin sheet molding compounds," *Polymer Composites*, vol. 1, no. 1, pp. 14–23, 1980. DOI: <https://doi.org/10.1002/pc.750010105>. eprint: <https://4spepublications.onlinelibrary.wiley.com/doi/pdf/10.1002/pc.750010105>.
- [19] C.-C. Lee and C. L. Tucker, "Flow and heat transfer in compression mold filling," *Journal of Non-Newtonian Fluid Mechanics*, vol. 24, no. 3, pp. 245–264, 1987. DOI: [https://doi.org/10.1016/0377-0257\(87\)80040-X](https://doi.org/10.1016/0377-0257(87)80040-X).
- [20] P. Odenberger, H. Andersson, and T. Lundström, "Experimental flow-front visualisation in compression moulding of SMC," *Composites Part A: Applied Science and Manufacturing*, vol. 35, no. 10, pp. 1125–1134, 2004. DOI: <https://doi.org/10.1016/j.compositesa.2004.03.019>.
- [21] C. L. Tucker III and F. Folgar, "A model of compression mold filling," *Polymer Engineering & Science*, vol. 23, no. 2, pp. 69–73, 1983. DOI: <https://doi.org/10.1002/pen.760230204>. eprint: <https://4spepublications.onlinelibrary.wiley.com/doi/pdf/10.1002/pen.760230204>.
- [22] S. G. Advani and C. L. Tucker III, "A numerical simulation of short fiber orientation in compression molding," *Polymer Composites*, vol. 11, no. 3, pp. 164–173, 1990. DOI: <https://doi.org/10.1002/pc.750110305>. eprint: <https://4spepublications.onlinelibrary.wiley.com/doi/pdf/10.1002/pc.750110305>.
- [23] C.-C. Lee, F. Folgar, and C. L. Tucker, "Simulation of Compression Molding for Fiber-Reinforced Thermosetting Polymers," *Journal of Engineering for Industry*, vol. 106, no. 2, pp. 114–125, 1984. DOI: [10.1115/1.3185921](https://doi.org/10.1115/1.3185921). eprint: [https://asmedigitalcollection.asme.org/manufacturingscience/article-pdf/106/2/114/6505535/114\\_1.pdf](https://asmedigitalcollection.asme.org/manufacturingscience/article-pdf/106/2/114/6505535/114_1.pdf).

- [24] M. R. Barone and T. A. Osswald, "A boundary element analysis of flow in sheet molding compound," *Polymer Composites*, vol. 9, no. 2, pp. 158–164, 1988. DOI: <https://doi.org/10.1002/pc.750090210>. eprint: <https://4spepublications.onlinelibrary.wiley.com/doi/pdf/10.1002/pc.750090210>.
- [25] T. A. Osswald and C. L. Tucker, "Compression Mold Filling Simulation for Non-Planar Parts," *International Polymer Processing*, vol. 5, no. 2, pp. 79–87, 1990. DOI: [doi:10.3139/217.900079](https://doi.org/10.3139/217.900079).
- [26] J. Görthofer *et al.*, "Virtual process chain of sheet molding compound: Development, validation and perspectives," *Composites Part B: Engineering*, vol. 169, pp. 133–147, 2019. DOI: <https://doi.org/10.1016/j.compositesb.2019.04.001>.
- [27] G. Alnersson, M. W. Tahir, A.-L. Ljung, and T. S. Lundström, "Review of the Numerical Modeling of Compression Molding of Sheet Molding Compound," *Processes*, vol. 8, no. 2, 2020. DOI: [10.3390/pr8020179](https://doi.org/10.3390/pr8020179).
- [28] Y. Li *et al.*, "Modeling and simulation of compression molding process for sheet molding compound (smc) of chopped carbon fiber composites," *SAE International Journal of Materials and Manufacturing*, vol. 10, no. 2, pp. 130–137, 2017. DOI: <https://doi.org/10.4271/2017-01-0228>.
- [29] N. Meyer, L. Schöttl, L. Bretz, A. Hrymak, and L. Kärger, "Direct Bundle Simulation approach for the compression molding process of Sheet Molding Compound," *Composites Part A: Applied Science and Manufacturing*, vol. 132, p. 105809, 2020. DOI: <https://doi.org/10.1016/j.compositesa.2020.105809>.
- [30] N. Meyer, "Mesoscale simulation of the mold filling process of Sheet Molding Compound," Ph.D. dissertation, Karlsruher Institut für Technologie, 2022.
- [31] G. Kotsikos and A. Gibson, "Investigation of the squeeze flow behaviour of Sheet Moulding Compounds (SMC)," *Composites Part A: Applied Science and Manufacturing*, vol. 29, no. 12, pp. 1569–1577, 1998. DOI: [https://doi.org/10.1016/S1359-835X\(98\)00094-3](https://doi.org/10.1016/S1359-835X(98)00094-3).
- [32] M. Hohberg, "Experimental investigation and process simulation of the compression molding process of Sheet Molding Compound (SMC) with local reinforcements," Ph.D. dissertation, Karlsruher Institut für Technologie (KIT), 2022, 184 pp. DOI: [10.5445/KSP/1000104914](https://doi.org/10.5445/KSP/1000104914).

- [33] K. T. Butler, D. W. Davies, H. Cartwright, O. Isayev, and A. Walsh, "Machine learning for molecular and materials science," *Nature*, vol. 559, no. 7715, pp. 547–555, 2018. DOI: 10.1038/s41586-018-0337-2.
- [34] M. Sourroubille, I. Y. Miranda-Valdez, T. Mäkinen, J. Koivisto, and M. J. Alava, "Thermogelation of methylcellulose: A rheological approach with Gaussian Process Regression," *Colloids and Surfaces A: Physicochemical and Engineering Aspects*, vol. 709, p. 136057, 2025. DOI: <https://doi.org/10.1016/j.colsurfa.2024.136057>.
- [35] M. Ziatdinov, Y. Liu, K. Kelley, R. Vasudevan, and S. V. Kalinin, "Bayesian Active Learning for Scanning Probe Microscopy: From Gaussian Processes to Hypothesis Learning," *ACS Nano*, vol. 16, no. 9, pp. 13492–13512, 2022, PMID: 36066996. DOI: 10.1021/acsnano.2c05303. eprint: <https://doi.org/10.1021/acsnano.2c05303>.
- [36] V. Torsti, T. Mäkinen, S. Bonfanti, J. Koivisto, and M. J. Alava, "Improving the mechanical properties of Cantor-like alloys with Bayesian optimization," *APL Machine Learning*, vol. 2, no. 1, p. 016119, 2024. DOI: 10.1063/5.0179844. eprint: [https://pubs.aip.org/aip/aml/article-pdf/doi/10.1063/5.0179844/19841923/016119\\_1\\_5.0179844.pdf](https://pubs.aip.org/aip/aml/article-pdf/doi/10.1063/5.0179844/19841923/016119_1_5.0179844.pdf).
- [37] S. M. Moosavi *et al.*, "A data-science approach to predict the heat capacity of nanoporous materials," *Nature Materials*, vol. 21, no. 12, pp. 1419–1425, 2022. DOI: 10.1038/s41563-022-01374-3.
- [38] T. Bayes and n. Price, "LII. An essay towards solving a problem in the doctrine of chances. By the late Rev. Mr. Bayes, F. R. S. communicated by Mr. Price, in a letter to John Canton, A. M. F. R. S.," *Philosophical Transactions of the Royal Society of London*, vol. 53, pp. 370–418, 1763. DOI: 10.1098/rstl.1763.0053. eprint: <https://royalsocietypublishing.org/doi/pdf/10.1098/rstl.1763.0053>.
- [39] J. Snoek, H. Larochelle, and R. P. Adams, "Practical Bayesian Optimization of Machine Learning Algorithms," in *Advances in Neural Information Processing Systems*, F. Pereira, C. Burges, L. Bottou, and K. Weinberger, Eds., vol. 25, Curran Associates, Inc., 2012.

- [40] B. Shahriari, K. Swersky, Z. Wang, R. P. Adams, and N. de Freitas, "Taking the Human Out of the Loop: A Review of Bayesian Optimization," *Proceedings of the IEEE*, vol. 104, no. 1, pp. 148–175, 2016. DOI: 10.1109/JPROC.2015.2494218.
- [41] P. I. Frazier, *A Tutorial on Bayesian Optimization*, 2018. arXiv: 1807.02811 [stat.ML].
- [42] C. E. Rasmussen and C. K. I. Williams, *Gaussian Processes for Machine Learning*. The MIT Press, 2006.
- [43] O. Kiss, "Bayesian Optimization for machine learning algorithms in the context of Higgs searches at the CMS experiment," Tech. Rep., 2019. arXiv: 1911.02501.
- [44] S. Ament, S. Daulton, D. Eriksson, M. Balandat, and E. Bakshy, *Unexpected Improvements to Expected Improvement for Bayesian Optimization*, 2025. arXiv: 2310.20708 [cs.LG].
- [45] R. Geissberger, J. Maldonado, N. Bahamonde, A. Keller, C. Dransfeld, and K. Masania, "Rheological modelling of thermoset composite processing," *Composites Part B: Engineering*, vol. 124, pp. 182–189, 2017. DOI: <https://doi.org/10.1016/j.compositesb.2017.05.040>.
- [46] "Thermosets," in *Engineered Materials Handbook Desk Edition*, ASM International, 1995. DOI: 10.31399/asm.hb.emde.a0003010. eprint: <https://dl.asminternational.org/handbooks/book/chapter-pdf/518495/a0003010.pdf>.
- [47] T. Sochi, "Slip at Fluid-Solid Interface," *Polymer Reviews*, vol. 51, no. 4, pp. 309–340, 2011. DOI: 10.1080/15583724.2011.615961. eprint: <https://doi.org/10.1080/15583724.2011.615961>.
- [48] M. Balandat *et al.*, "BoTorch: A Framework for Efficient Monte-Carlo Bayesian Optimization," in *Advances in Neural Information Processing Systems 33*, 2020.
- [49] C. R. Harris *et al.*, "Array programming with NumPy," *Nature*, vol. 585, no. 7825, pp. 357–362, 2020. DOI: 10.1038/s41586-020-2649-2.
- [50] R. Preece and J. Milanović, "Efficient Estimation of the Probability of Small-Disturbance Instability of Large Uncertain Power Systems," *IEEE Transactions on Power Systems*, vol. 31, pp. 1–10, 2015. DOI: 10.1109/TPWRS.2015.2417204.
- [51] M. Binois and R. B. Gramacy, "hetGP: Heteroskedastic Gaussian Process Modeling and Sequential Design in R," *Journal of Statistical Software*, vol. 98, no. 13, pp. 1–44, 2021. DOI: 10.18637/jss.v098.i13.

- [52] L. M. Kimpton, M. Dunne, J. M. Salter, and P. Challenor, “Cross-validation-based sequential design for stochastic models,” *Philosophical Transactions of the Royal Society A: Mathematical, Physical and Engineering Sciences*, vol. 383, no. 2293, p. 20240217, 2025. DOI: 10.1098/rsta.2024.0217. eprint: <https://royalsocietypublishing.org/doi/pdf/10.1098/rsta.2024.0217>.
- [53] N. Kluge, T. Lundström, L.-G. Westerberg, and K. Olofsson, “Compression moulding of sheet moulding compound: Modelling with computational fluid dynamics and validation,” *Journal of Reinforced Plastics and Composites*, vol. 34, pp. 479–492, 2015. DOI: 10.1177/0731684415573981.
- [54] D. Ferré-Sentis, P. Dumont, L. Orgéas, F. Martoia, and M. Sager, “Rheological response of compressible SMCs under various deformation kinematics: Experimental aspects and simple modelling approach,” *Composites Part A: Applied Science and Manufacturing*, vol. 154, p. 106774, 2022. DOI: <https://doi.org/10.1016/j.compositesa.2021.106774>.
- [55] F. Rothenhäusler *et al.*, “Experimental and Numerical Analysis of SMC Compression Molding in Confined Regions—A Comparison of Simulation Approaches,” *Journal of Composites Science*, vol. 6, no. 3, 2022. DOI: 10.3390/jcs6030068.
- [56] I. Y. Miranda-Valdez, T. Mäkinen, J. Koivisto, and M. J. Alava, *Bayesian optimization to infer parameters in viscoelasticity*, 2025. arXiv: 2502.19132 [cond-mat.soft].